12-10-2010

Density functional theory and modified embedded-atom method: applications to steel, magnesium alloys, and semiconductor surfaces

Jeff Lynn Houze

DENSITY FUNCTIONAL THEORY AND MODIFIED EMBEDDED-ATOM METHOD: APPLICATIONS TO STEEL, MAGNESIUM ALLOYS, AND SEMICONDUCTOR SURFACES

By

Jeff Houze

A Dissertation
Submitted to the Faculty of
Mississippi State University
in Partial Fulfillment of the Requirements
for the Degree of Doctorate of Philosophy
in Computational Engineering
in the Department of Computational Engineering

Mississippi State, Mississippi

December 2010

DENSITY FUNCTIONAL THEORY AND MODIFIED EMBEDDED-ATOM METHOD: APPLICATIONS TO STEEL, MAGNESIUM ALLOYS, AND SEMICONDUCTOR SURFACES

By

Jeff Houze

Approved:

Seong-Gon Kim Associate Professor of Physics and Astronomy (Major Professor)	Mark Novotny Professor of Physics and Astronomy and Department Head (Committee Member)
Ioana Banicescu Professor of Computer Science and Engineering (Committee Member)	Hyeona Lim Associate Professor of Mathematics (Committee Member)
Mark F. Horstemeyer Professor of Mechanical Engineering (Committee Member)	Roger King Giles Distinguished Professor of Electrical and Computer Engineering (Graduate Coordinator)

Sarah A. Rajala
Dean of the James Worth Bagley
College of Engineering and Professor

Name: Jeff Houze

Date of Degree: December 10, 2010

Institution: Mississippi State University

Major Field: Computational Engineering

Major Professor: Dr. Seong-Gon Kim

Title of Study: DENSITY FUNCTIONAL THEORY AND MODIFIED EMBEDDED-ATOM METHOD: APPLICATIONS TO STEEL, MAGNESIUM ALLOYS, AND SEMICONDUCTOR SURFACES

Pages in Study: 82

Candidate for Degree of Doctorate of Philosophy

We performed atomistic modeling to study structural and mechanical properties of materials. We used density functional theory (DFT) for all the studies presented and constructed a method for quickly optimizing semi-empirical modified embedded atom method (MEAM) potentials.

In our first study, we show that the reconstruction model in the literature for GaSb(001) is not predicted to have the lowest surface reconstruction energy. A modification was proposed that improves the energy. The second study tries to validate a crystal structure for the Φ Phase of Al-Mg-Zn. The third study deals with plain carbon steel, including some microalloying of Vanadium and vacancy assisted diffusion of Fe in Cementite(Fe_3C). In the fourth study, we show a method for optimizing a MEAM potential. The code written is specific to hexagonal closed packed structures and was applied to a Magnesium potential.

TABLE OF CONTENTS

LIST OF TABLES v

LIST OF FIGURES vi

CHAPTER

1. INTRODUCTION 1

1.1 Introduction 1
1.2 Application 2
1.2.1 Crystal Defects 3
1.2.2 Potentials 3
1.2.3 III-V Semiconductor Surfaces 4
1.2.4 Al-Mg-Zn 5
1.2.5 Steel 5
1.3 Contributions 6

2. THEORY: DFT AND (M)EAM 8

2.1 Introduction 8
2.1.1 Born-Oppenheimer Approximation 8
2.1.2 Hohenberg-Kohn Theorem 9
2.1.3 Density Functional Theory 9
2.1.3.1 Local Density Approximation 9
2.1.3.2 Generalized Gradient Approximation 10
2.1.3.3 Pseudo-potential 10
2.1.3.4 Basis Set 11
2.2 Semi-empirical Potentials 11
2.2.1 EAM 12
2.2.2 Finnis-Sinclair Form 13
2.2.3 MEAM 14

3. GASB(001) AND ALSB(001) 18

3.1 Introduction 18

3.2 Methods . . . 21
3.3 Results and Discussions . . . 23
3.4 Summary and Conclusions . . . 34

4. AL-MG-ZN TERNARY Φ PHASE . . . 35

4.1 Introduction . . . 35
4.2 Computational Method . . . 37
4.3 Results . . . 37
4.4 Conclusion . . . 43

5. STEEL . . . 45

5.1 Introduction . . . 45
5.2 Point Defect Energies In Cementite . . . 48
5.3 Diffusion Barrier Calculations . . . 49

6. MEAM OPTIMIZATION . . . 53

6.1 Introduction . . . 54
6.1.1 Multi-objective Optimization . . . 57
6.2 Potential Construction Procedure . . . 58
6.2.1 Cohesive Energies . . . 60
6.2.2 Elastic Constants . . . 61
6.2.3 Surface Formation Energies . . . 61
6.2.4 Stacking Fault Energies . . . 63
6.2.5 Vacancy Formation Energies . . . 64
6.2.6 Atomic Forces . . . 64
6.3 Results and Discussion . . . 65
6.3.1 Material Properties . . . 65
6.3.2 Additional Material Properties . . . 69
6.3.3 Thermal Properties . . . 71
6.4 Conclusions . . . 72

7. CONCLUSION . . . 74

7.1 Summary . . . 74
7.2 Future Direction . . . 75

REFERENCES . . . 75

LIST OF TABLES

3.1 Electron count for different reconstructions of the GaSb(001) surface 24

4.1 Statistics of ΔE_{rel} for the 10 (Al,Zn) sites 40

4.2 Lattice constants and internal parameters of optimal structure 42

5.1 Bulk Fe energies for different potentials, phases, and magnetic setting 45

5.2 Cementite unit cell structure 47

5.3 Internal parameters of Cementite 48

5.4 Defect formation energies in Cementite (eV) 50

5.5 Diffusion into Fe(I) site of Fe(7) in Cementite 52

5.6 Diffusion into Fe(II) site of Fe(40) in Cementite 52

6.1 Bulk properties optimized to construct the MEAM potential 60

6.2 Elastic constants comparison of optimized MEAM potential 62

6.3 2-D and 1-D defect formation energies 63

6.4 Force based optimizations 66

6.5 Optimized set of MEAM potential parameters for Mg 66

6.6 Unoptimized material properties of the Mg potential 69

LIST OF FIGURES

3.1 Proposed reconstruction models with (4×3) and (4×4) periodicities 25

3.2 Proposed reconstruction models for the GaSb(001)-(1×5)-like surfaces 26

3.3 Reconstruction models with a single substitution of Sb atoms by Ga atoms . . 27

3.4 Reconstruction models with a double substitution of Sb atoms by Ga atoms . 28

3.5 Surface stability phase diagram for AlSb(001) surfaces 29

3.6 Surface stability phase diagram for GaSb(001) surfaces 30

3.7 Filled-state STM images of GaSb(001) with (1×5) periodicity 32

4.1 Relative Stability of $Mg_{84}(Al_x, Zn_{1\text{-}x})_{68}$ using the tie line concept 38

4.2 Relative stability energy comparing Al or Zn in Site 2 39

4.3 Differences in relative stability of listed site being occupied by Al or Zn . . . 40

4.4 Connections to lowest energy configuration 44

5.1 Fe-C phase diagram 46

5.2 Vanadium substitution in Cementite 49

5.3 Fe diffusion in Cementite 51

6.1 Cohesive energies computed from potential compared to Rose eq 68

6.2 Energy vs temperature for the Mg potential 73

CHAPTER 1

INTRODUCTION

1.1 Introduction

The performance of modern processors makes solving reasonable approximations of practical systems possible. Even *ab initio* methods which derive directly from first principles can be employed to produce useful results when experimental results are lacking or unreliable. For some systems like surface reconstructions or simple point defect calculations Density functional theory (DFT) is especially well suited, and can provide the complete solution. The main limitation of these methods is the size of the systems that can be investigated, and they are especially inept at doing anything requiring dynamics since the computational time required for each step is so long. They can be used when the motion is constrained as in finding minimum energy paths and calculating generalized stacking faults. The latter might take a day and mere seconds using an embedded atom method (EAM) potential. The benefit is that the *ab initio* results are reliable not requiring fitting of any parameters. As such they are used to fit the EAM potentials.

The ultimate goal of electronic structure calculations would be to solve the Schrödinger equation $\hat{H}\Psi = E\Psi$, for a many body system of interest. $\hat{H}$ is the Hamiltonian operator for the wave-function Ψ and E is the total energy of the system. This is, however, unfeasible for more than the simplest atoms. With the Hohenburg-Kohn (H-K)

theorems and some reasonable approximations very good results can be achieved with Density Functional Theory. The H-K theorems reduce solving a 3×N dimensional wave-function where N is the number of electrons to a 3 /dimensional electron density problem. They establish that minimizing the density functional obtains the ground-state density, and that this density uniquely determines all properties of the system including the wave-function. With more accurate functionals the theory has become a popular method in computational physics and chemistry. For instance the generalized gradient approximation for the exchange-correlation (XC) energy functional is required to correctly predict the crystal structure of iron. Despite the improvements in accuracy DFT still requires a lot of computer time compared to semi-empirical methods.

Using the DFT code VASP the total number of atoms is limited to around 400 before it simply crashes on the raptor cluster. Other codes like Siesta claim to handle thousands of atoms, but semi-empirical inter-atomic potential method codes can handle a few million atoms. Two popular potential types are the embedded atom method (EAM) and the modified embedded atom method (MEAM) extended from EAM to handle angular dependencies. MEAM potentials when fitted well can produce realistic structural properties.

1.2 Application

Valence electrons dominate atomic bonding in crystals, in addition to molecules, which partially explains why Vanadium and Niobium would have similar effects in microalloying of steel. They both have 5 valence electrons and are in the same column on

the periodic table. The Alkali metals all have a single valence electron and are highly reactive while the noble gases have full shells containing either 2, 8, or 18 electrons as s,p, and d orbitals come into existence are chemically inert. The alkali metals Sodium (Na), Potassium (K), and Cesium (Cs) all with one valence electron form crystals with Chlorine, which being only one electron short from having a full shell, in 1 to 1 ratios. What is more interesting is that these all are different crystal structures, and can be correctly predicted by *ab initio* methods.

1.2.1 Crystal Defects

Defects naturally occur in crystals, ranging from point defects to grain boundaries. The simplest being point defects including: vacancies, interstitials, impurities, and substitutional defects. All of which can be easily calculated with DFT and then used in developing semi-empirical potentials. More complicated planar defects when using periodic boundary conditions such as surfaces and stacking faults are also good points for comparison. Defects including grain boundaries, dislocations, voids, and precipitates generally require too many atoms for DFT simulations, but are nonetheless necessary to study by other means including with MEAM potentials to understand mechanical properties of materials.

1.2.2 Potentials

VASP supplies the potentials for most elements in ultrasoft pseudopotentials (USPP) or Projector-Augmented Wave (PAW) format describing the interaction between

ions and electrons. Both formats also have local density approximation (LDA) or generalized gradient approximation (GGA) versions for describing the exchange-correlation energy functional. The great thing about DFT is that one is free to combine different element potentials together for multi-element simulations.

With MEAM it requires more fitting to describe the interactions of the pair potentials. It was possible to make a carbon interstitial prefer the tetrahedral position instead of the correct octahedral position. This is not possible within DFT, barring user error or some serious bug in the code.

For the study of the Φ phase of Al-Mg-Zn using DFT was a natural choice for reliably calculating the energy of the system in different configurations. Now using these results along with the τ phase calculated by my colleague one could develop a reasonable MEAM potential for Al-Mg-Zn.

1.2.3 III-V Semiconductor Surfaces

We used DFT to study the structure of AlSb(001) and GaSb(001) surfaces. The GaSb(001) reconstruction in the Sb rich case is unique among all other arsenide and antimonide III-V compounds. The other compounds form a c(4x4) reconstruction which is shown correctly as energetically favored for AlSb. The same c(4x4) is also predicted for GaSb(001) rather than the structural model resembling the experimental scanning tunneling microscope image.

1.2.4 Al-Mg-Zn

The Φ phase is one of two established ternary phases of Al-Mg-Zn alloys [79]. Bourgeois et al.[10] proposed a crystal structure, and validated it by comparing calculated electron diffraction patterns with experiment. They also established the space group as Pbcm. They could not completely resolve whether some sites were Al or Zn. We aimed to use DFT predictive capabilities to determine which sites should be occupied by Al and which by Zn.

1.2.5 Steel

Plain carbon steel mainly consists of iron with small amounts of carbon. Other elements may be alloyed for different mechanical responses, and environmental reasons. Stainless steel for example contains sufficient amounts of chromium that a passive layer of chromium oxide forms on the surface. This prevents the iron from oxidizing in a process better known as rusting. Iron occurs in two crystal structures dependent of temperature. The first is ferrite a body-centered cubic crystal below 910 °C and again above 1390 °C until the melting point of 1536 °C. The lower temperature range is called alpha-iron and the high temperature range delta-iron. Between 910 °C and 1390 °C iron transforms into Austenite a face centered cubic crystal.

Carbon also commonly occurs in the two crystal structures, diamond and graphene. They are both ground state structures existing over wide temperature ranges. Carbon also can be manipulated with modern technology to form fullerenes and nanotubes. For the

purpose of studying steel we are only concerned with how atoms of carbon harden relatively soft pure iron.

Carbon atoms are smaller than iron, and occupy the interstices of ferrite and austenite. Ferrite is more loosely packed than austenite. The larger holes that occur in austenite, however, leads it to being able to solute an order of magnitude more carbon.

Carbon is of sufficient size that it distorts the surrounding lattice, and actually prefers to occupy the octahedral positions displacing two neighboring Fe atoms than the initially larger tetrahedral interstitial site where displacing the four nearest neighbors would actually cost more energy. The maximum carbon solubility in austenite is just over 2 percent by weight or 9.1 atomic percent Carbon at 1,150 °C. In ferrite the solubility is only 0.1 atomic percent at 723 °C.

The maximum amount of carbon with iron is 25 atomic percent in the form of Cementite(Fe_3C) the most stable carbide of iron. It is, however, only metastable with respect to ferrite and graphite. Cementite is a hard, brittle material. Vacancy assisted diffusion barriers of iron in Cementite using a climbing image nudged elastic band method will be presented.

1.3 Contributions

We were the first to suggest that Ga subsurface atoms stabilize the GaSb(001) (nx5)-like surface reconstructions. This theory has since been supported by experimental reflectance anisotropy spectra [33]. We explored the ternary Φ phase of Al-Mg-Zn alloy using total energy calculations to resolve atomic occupancies that were thus far unresolved.

This will be useful in developing a ternary (M)EAM potential in the future. Vacancy assisted diffusion barriers within Cementite were calculated. This revealed fifteen different barriers ranging from 0.59 eV to 2.23 eV. A series of scripts were written that take parameters a MEAM potential any quickly calculate many properties for an hcp crystal. This was combined with a simple optimizer to optimize a Mg MEAM potential.

CHAPTER 2

THEORY: DFT AND (M)EAM

2.1 Introduction

The theoretical foundation of Density Functional Theory (DFT) was born in the mid 1960s. Walter Kohn established that knowledge of the density distribution of the electrons has implicit in it all the specific properties of a system including the solution of the Schrödinger equation. This chapter will cover the assumptions and methods used in DFT calculations.

2.1.1 Born-Oppenheimer Approximation

The Born-Oppenheimer approximation is ubiquitous in all electronic structure calculations. Owing to the fact the nuclei of atoms are orders of magnitude heavier than the orbiting electrons, it's possible to decouple the wavefuctions of the nuclei from the electronic wavefuctions. When solving the electronic wavefuction the nuclei are considered fixed in place providing a static potential field due to Coulomb interactions.

2.1.2 Hohenberg-Kohn Theorem

The first theorem states that the ground state properties are uniquely determined by the electron density $n(r)$. The second theorem defines an energy functional of the density $E[n(r)]$ that when minimized is the electron density for the ground state.

2.1.3 Density Functional Theory

In the Kohn-Sham approach to density functional theory the density to be solved is defined in terms of Kohn-Sham orbitals. Variational methods applied to these orbitals determine the effective potential. Inherent in determining the potential lies the exchange-correlation energy which is not known exactly and must be approximated. Many approximations to the exchange-correlation functional exist. Most notably the local density approximation (LDA) and the generalized gradient approximation (GGA).

2.1.3.1 Local Density Approximation

The local density approximation (LDA) assumes that the exchange-correlation energy is only determined by the local electron density as

$$E_{xc}[n(r)] = \int n(r)\epsilon_{xc}[n(r)]\, dr. \tag{2.1}$$

The $\epsilon_{xc}[n(r)]$ is an energy per electron that only depends on the density $n(r)$ close to the point r. Since the exchange-correlation functional $E_{xc}[n(r)]$ is universal, it could be the same as the one for a homogeneous electron gas. If this is true, the exchange part

has an analytical form. The correlation part was calculated by Ceperley and Alder using Monte-Carlo methods [15].

2.1.3.2 Generalized Gradient Approximation

In contrast to the LDA equation, the generalized gradient approximation (GGA) includes the gradient of the electron density when evaluating the exchange-correlation energy, and is given by

$$E_{xc}[n(r), \nabla n(r)] = \int n(r)\epsilon_{xc}[n(r), \nabla n(r)]\, dr. \tag{2.2}$$

The parametrization of GGA include those of Perdew-Wang (PW91) and Perdew-Burke-Ernzerhof (PBE). They are two different functionals to represent the gradient of electron densities, we use PBE in our calculations.

2.1.3.3 Pseudo-potential

The electrons close to an atomic core are much less affected by surrounding atoms than are the valence electrons. Assuming the core electrons and core are fixed, a pseudo-potential approach replaces the combined effects of the core electrons and Coulomb potential from the atomic core by a single pseudo-potential that acts only on the valence electrons. The resulting pseudo-wave functions of the valence electrons are then smoother and the number of plane-waves required to represent them is lower, resulting in faster convergence of the total energy with respect to the plane-wave energy cutoff. For r less than the cutoff radius r_c, the full wave function and pseudo-wave function match each other.

The norm conservation condition ensures that pseudo-wave functions and all electron wave functions generate the same charge densities. Ultrasoft pseudo-potentials introduced later do not impose the norm conservation constrain, providing the benefit of softer wave functions and smaller cutoff radii than the norm conserving pseudo-potentials. A certain drawback of pseudo-potentials is due to the nonlinearity of the exchange-correlation functional in DFT, elaborate nonlinear core corrections are required for an accurate description of valence-core interaction in all systems where the overlap between core and valence electron densities is not negligible. The Projector-Augmented Wave (PAW) approach developed by Blöchl reconstructs the full all-electron density and avoids the necessity of non linear core-corrections.

2.1.3.4 Basis Set

In practice, the Kohn-Sham equations are solved iteratively, using an expansion of the orbitals in an appropriately chosen set of basis functions. The plane-wave (PW) basis-set adopted in VASP offers two main advantages: (a) control of basis set convergence; and (b) the calculation of the forces acting on the atoms and of the stresses on the unit cell using the Hellmann-Feynman theorem [25]. The last advantage opens the way to quantum *ab initio* molecular dynamic simulations to understand the time evolution of a system.

2.2 Semi-empirical Potentials

The modified-embedded-atom method (MEAM) proposed by Baskes et al [4, 5, 6] is one of the most widely used methods using semi-empirical atomic potentials to date.

The MEAM is based on the embedded-atom method (EAM) [3, 17, 18, 19] and extended to include angular forces. The MEAM and EAM use a single formalism to generate semi-empirical potentials that have been successfully applied to a large variety of materials including fcc, bcc, hcp, diamond-structured materials and even gaseous elements, to produce simulations that are in good agreement with experiments or first-principles calculations.

2.2.1 EAM

Within the EAM approach, the total energy E of a system of atoms is written as the sum of the atomic energies

$$E = \sum_i E_i. \tag{2.3}$$

The atomic energy is the sum of two contributions:

$$E_i = F^{t_i}(n_i) + \frac{1}{2}\sum_{j \neq i} V^{t_i t_j}(r_{ij}) \tag{2.4}$$

where the subscript i and j label distinct atoms, r_{ij} is the separation between atoms i and j, and t_i is the element type of atom i. $V(r)$ is an interatomic pairwise potential and $F^{t_i}(n_i)$ is the embedding-energy function of element type t_i as a function of the local "atomic density" at the site of atom i

$$n_i = \sum_{j \neq i} \rho^{t_j}(r_{ij}) \tag{2.5}$$

where $\rho^{t_j}(r)$ is the "atomic density" around an isolated atom of element type t_j. The embedding energy $F^{t_i}(n_i)$ represents the energy cost to insert atom i of element type t_i at a site where the atomic density is n_i. For a binary alloy with element types A and B, the

EAM requires seven functions to be determined: $F^A(n)$, $F^B(n)$, $\rho^A(r)$, $\rho^B(r)$, $V^{AA}(r)$, $V^{BB}(r)$, and $V^{AB}(r)$. Six of these functions can be determined using properties of the pure components while the cross function $V^{AB}(r)$ should be fitted to alloy properties. Typically, these functions are fitted to reproduce a few bulk properties (such as lattice constant, cohesive energy, elastic constants) and surface and simple defect properties (such as surface-formation energy and vacancy-formation energy).

2.2.2 Finnis-Sinclair Form

Finnis and Sinclair (FS) extended the EAM potential to be more flexible by allowing the "atomic density" to be environment-dependent [26]:

$$n_i = \sum_{j \neq i} \rho^{t_i t_j}(r_{ij}). \tag{2.6}$$

For a binary alloy with atom types A and B, the FS potential requires eight functions to be determined: $F^A(n)$, $F^B(n)$, $\rho^{AA}(r)$, $\rho^{BB}(r)$, $\rho^{AB}(r)$, $V^{AA}(r)$, $V^{BB}(r)$, and $V^{AB}(r)$. Six of these functions can be determined using properties of the pure components while the cross functions $\rho^{AB}(r)$, and $V^{AB}(r)$ should be fitted to alloy properties. The V-Fe potential by Mendelev and co-workers [66] is one of the best examples of semi-empirical interatomic potentials in the FS form.

2.2.3 MEAM

In MEAM, all functions of EAM potentials are represented in analytical forms. The embedding energy is given in the form

$$F^{t_i}(n_i) = A_{t_i} E^0_{t_i} n_i \ln(n_i), \tag{2.7}$$

where the parameters $E^0_{t_i}$ and A_{t_i} depend on the element type t_i of atom i. The atomic density n_i is given by

$$n_i = \frac{\rho_i^{(0)}}{\rho_i^0} G(\Gamma_i), \tag{2.8}$$

where

$$\Gamma_i = \sum_{k=1}^{3} \bar{t}_i^{(k)} \left(\frac{\rho_i^{(k)}}{\rho_i^{(0)}} \right)^2 \tag{2.9}$$

and

$$G(\Gamma_i) = \sqrt{1 + \Gamma_i}. \tag{2.10}$$

The zeroth and higher order densities, $\rho_i^{(0)}$, $\rho_i^{(1)}$, $\rho_i^{(2)}$, and $\rho_i^{(3)}$ are given later in Eq. (2.13). The composition-dependent electron density scaling ρ_i^0 is given by

$$\rho_i^0 = \rho_{i0} Z_{i0} G(\Gamma_i^{\text{ref}}), \tag{2.11}$$

where ρ_{i0} is an element-dependent density scaling, Z_{i0} is the first nearest-neighbor coordination of the reference system, and Γ_i^{ref} is given by

$$\Gamma_i^{\text{ref}} = \frac{1}{Z_{i0}^2} \sum_{k=1}^{3} \bar{t}_i^{(k)} s_i^{(k)}, \tag{2.12}$$

where $s_i^{(k)}$ is the shape factor that depends on the reference structure for atom i. Shape factors for various structures are specified in the work of Baskes [4]. The partial electron densities are given by

$$\rho_i^{(0)} = \sum_{j \neq i} \rho_j^{a(0)} S_{ij} \tag{2.13a}$$

$$\left(\rho_i^{(1)}\right)^2 = \sum_{\alpha} \left[\sum_{j \neq i} \rho_j^{a(1)} \frac{r_{ij\alpha}}{r_{ij}} S_{ij} \right]^2 \tag{2.13b}$$

$$\begin{aligned} \left(\rho_i^{(2)}\right)^2 = & \sum_{\alpha,\beta} \left[\sum_{j \neq i} \rho_j^{a(2)} \frac{r_{ij\alpha} r_{ij\beta}}{r_{ij}^2} S_{ij} \right]^2 \\ & - \frac{1}{3} \left[\sum_{j \neq i} \rho_j^{a(2)} S_{ij} \right]^2 \end{aligned} \tag{2.13c}$$

$$\begin{aligned} \left(\rho_i^{(3)}\right)^2 = & \sum_{\alpha,\beta,\gamma} \left[\sum_{j \neq i} \rho_j^{a(3)} \frac{r_{ij\alpha} r_{ij\beta} r_{ij\gamma}}{r_{ij}^3} S_{ij} \right]^2 \\ & - \frac{3}{5} \sum_{\alpha} \left[\sum_{j \neq i} \rho_j^{a(3)} \frac{r_{ij\alpha}}{r_{ij}} S_{ij} \right]^2, \end{aligned} \tag{2.13d}$$

where $r_{ij\alpha}$ is the α component of the displacement vector from atom i to atom j. S_{ij} is the screening function between atoms i and j and is defined later in Eqs. (2.20). The atomic electron densities are computed as

$$\rho_i^{a(k)}(r_{ij}) = \rho_{i0} \exp\left[-\beta_i^{(k)}\left(\frac{r_{ij}}{r_i^0} - 1\right)\right], \tag{2.14}$$

where r_i^0 is the nearest-neighbor distance in the single-element reference structure and $\beta_i^{(k)}$ are element-dependent parameters. Finally, the average weighting factors are given by

$$\bar{t}_i^{(k)} = \frac{1}{\rho_i^{(0)}} \sum_{j \neq i} t_j^{(k)} \rho_j^{a(0)} S_{ij}, \tag{2.15}$$

where $t_j^{(k)}$ is an element-dependent parameter.

The pair potential is given by

$$\phi_{ij}(r_{ij}) = \bar{\phi}_{ij}(r_{ij}) S_{ij} \tag{2.16}$$

$$\begin{aligned}\bar{\phi}_{ij}(r_{ij}) = \frac{1}{Z_{ij}} \Bigg[& 2E_{ij}^u(r_{ij}) - F_i\left(\frac{Z_{ij}\rho_j^{(0)}(r_{ij})}{Z_i \rho_i^0}\right) \\ & - F_j\left(\frac{Z_{ij}\rho_i^{(0)}(r_{ij})}{Z_j \rho_j^0}\right)\Bigg]\end{aligned} \tag{2.17}$$

$$E_{ij}^u(r_{ij}) = -E_{ij}^0\left(1 + a_{ij}^*(r_{ij})\right) e^{-a_{ij}^*(r_{ij})} \tag{2.18}$$

$$a_{ij}^* = \alpha_{ij}\left(\frac{r_{ij}}{r_{ij}^0} - 1\right), \tag{2.19}$$

where α_{ij} is an element-dependent parameter. The sublimation energy E_{ij}^0, the equilibrium nearest-neighbor distance r_{ij}^0, and the number of nearest-neighbors Z_{ij} are obtained from

the reference structure. E^u is the universal equation of state (EOS) from Rose et al [80] and choosing the pair potential this way reproduces the behavior of the reference state under homogeneous compression and expansion.

The screening function S_{ij} is designed so that $S_{ij} = 1$ if atoms i and j are unscreened and within the cutoff radius r_c, $S_{ij} = 0$ if they are completely screened or outside the cutoff radius, and varies smoothly between 0 and 1 for partial screening. The total screening function is the product of a radial cutoff function and three-body terms involving all other atoms in the system:

$$S_{ij} = \bar{S}_{ij} f_c\left(\frac{r_c - r_{ij}}{\Delta r}\right) \tag{2.20a}$$

$$\bar{S}_{ij} = \prod_{k \neq i,j} S_{ikj} \tag{2.20b}$$

$$S_{ikj} = f_c\left(\frac{C_{ikj} - C_{\text{min},ikj}}{C_{\text{max},ikj} - C_{\text{min},ikj}}\right) \tag{2.20c}$$

$$C_{ikj} = 1 + 2\frac{r_{ij}^2 r_{ik}^2 + r_{ij}^2 r_{jk}^2 - r_{ij}^4}{r_{ij}^4 - \left(r_{ik}^2 - r_{jk}^2\right)^2} \tag{2.20d}$$

$$f_c(x) = \begin{cases} 1 & x \geq 1 \\ \left[1 - (1-x)^4\right]^2 & 0 < x < 1 \\ 0 & x \leq 0 \end{cases} \tag{2.20e}$$

Note that C_{min} and C_{max} can be defined separately for each i-j-k triplet, based on their element types. The parameter Δr controls the distance over which the radial cutoff function changes from 1 to 0 near $r = r_c$. Further note that the radial cutoff is used for computational convenience and r_c is chosen so that the results do not depend on it.

CHAPTER 3

GASB(001) AND ALSB(001)

We use density-functional theory to study the structure of AlSb(001) and GaSb(001) surfaces. Based on a variety of reconstruction models, we construct surface stability diagrams for AlSb and GaSb under different growth conditions. For AlSb(001), the predictions are in excellent agreement with experimentally observed reconstructions. For GaSb(001), we show that the previously proposed model accounts for the experimentally observed reconstructions under Ga-rich growth conditions, but fails to explain the experimental observations under Sb-rich conditions. We propose a new model that has a substantially lower surface energy than all ($n\times5$)-like reconstructions proposed previously and that, in addition, leads to a simulated STM image in better agreement with experiment than existing models. However, this new model has higher surface energy than some of the (4×3)-like reconstructions, models with periodicity that has not been observed. Hence we conclude that the experimentally observed (1×5) and (2×5) structures on GaSb(001) are kinetically limited rather than at the ground state.

3.1 Introduction

The surfaces and interfaces of III-V semiconductors constitute some of the most important components of the semiconductor industry. For example, III-V heterostructure

quantum wells are key components in a wide range of optical and high-frequency electronic devices, including field-effect transistors [41], resonant tunneling structures [44], infrared lasers [63], and infrared detectors [23]. Many of these devices require extremely sharp and clean interfaces. For this reason, an understanding of the atomic-scale morphology of III-V semiconductor surfaces is critical to controlling the growth and formation of their interfaces [16, 28].

It is generally accepted that the surfaces of III-V semiconductors should reconstruct in such a way that the number of electrons is exactly enough to doubly occupy all orbitals on electronegative (V) atoms, leaving all orbitals on electropositive (III) atoms unoccupied. This guiding principle, known as the electron-counting model (ECM), has been used to screen candidate structural models of many observed reconstructions on the surfaces of III-V semiconductors [11, 14, 43, 62, 81]. In practice, however, not all experimentally realized reconstructions follow this principle. For example, under Sb-rich growth conditions, GaSb(001) forms surface reconstructions that are weakly metallic and hence violate the ECM [55], even though the closely related AlSb(001) surface forms insulating reconstructions that satisfy it [89]. The nature of reconstructions that violate the ECM, and the underlying reasons for their stability, are thus important for understanding III-V surfaces in general.

In this article we explore theoretically a large number of judiciously chosen candidate reconstructions on GaSb(001) and AlSb(001). We find that as the growth conditions are varied between Sb-poor and Sb-rich, the predicted sequence of stable reconstructions for GaSb(001) is exactly analogous to those of AlSb(001). Experimentally, however, the

picture is more complicated. In the Sb-poor limit, the observed GaSb(001) reconstruction is indeed analogous to that of AlSb(001). On the other hand, in the Sb-rich limit, the experimentally observed reconstructions for GaSb(001) and AlSb(001) are different. Moreover, in this limit the predicted and observed reconstructions are in good agreement only for AlSb(001), while for GaSb(001) there remains an unresolved discrepancy between theory and experiment.

Experimentally, the Sb-terminated AlSb(001) surface evolves through the sequence $\alpha(4\times3) \rightarrow \beta(4\times3) \rightarrow \gamma(4\times3) \rightarrow$ c(4×4) as the growth condition is changed from low Sb flux (or high substrate temperature) to high Sb flux (or low temperature) [89]. All of these reconstructions are insulating, and are well accounted for by structural models proposed in the literature that satisfy the ECM.

Of particular interest here is the Sb-rich AlSb(001)-$c(4\times4)$ reconstruction, analogous to the As-rich GaAs(001)-$c(4\times4)$ reconstruction, which is observed on AlSb but not GaSb. In contrast to both AlSb and GaAs, the GaSb(001) surface does not exhibit a stable, insulating $c(4\times4)$ reconstruction under similar—or any other—growth conditions. Instead, it forms $(n\times5)$-like reconstructions [27, 40, 55, 64, 69]. Structural models proposed in the literature for these $(n\times5)$-like reconstructions violate, by design, the ECM and consequently are weakly metallic [55]. Simulated scanning tunneling microscopy (STM) images based on (2×10) and $c(2\times10)$ models closely resemble the experimental images [55]. As a result, these models have been generally accepted as describing the GaSb(001) surface under Sb-rich growth conditions. Nevertheless, we show below on energetic grounds that these models are unlikely to be correct. Specifically, we find

their calculated surface energy to be significantly higher than GaSb(001)-$c(4\times4)$ for any plausible value of Sb chemical potential. However, since the experimentally observed reconstruction of GaSb(001) does not have $c(4\times4)$ periodicity, this model cannot be correct either. Thus a definitive structural model remains to be found.

3.2 Methods

The basic structural models we considered are taken from the literature and are shown in Figs. 3.1 and 3.2. Surfaces that satisfy the ECM are generally semiconducting, while those that do not may be metallic. The degree to which a given surface satisfies the ECM can be measured by the excess electron count, $\Delta\nu$, which we define here as the difference between the number of available electrons and the number required to satisfy the ECM, per (1×1) surface unit cell. Excess electron counts for the structural models in Figs. 3.1 and 3.2 are tabulated in Table 3.1.

To compare the surface energies of reconstruction models with different periodicities and stoichiometries, we consider the surface energy per unit area,

$$\gamma = E_{\text{surf}}/A = (E_{\text{tot}} - n_{\text{III}}\mu'_{\text{III}} - n_{\text{V}}\mu'_{\text{V}})/A, \tag{3.1}$$

where E_{tot} is the total energy of a reconstructed surface, of area A, containing n_{III} group-III and n_{V} group-V adatoms in excess with respect to the bulk-truncated, Sb-terminated AlSb(001) or GaSb(001). The atomic chemical potentials μ' are more conveniently expressed in terms of excess chemical potentials μ, relative to the energy per atom in the

ground-state elemental phases: $\mu' = \mu^{\text{bulk}} + \mu$. Assuming the surface to be in thermodynamic equilibrium with the bulk, the III and V chemical potentials are related by μ_{III} + μ_{V} = ΔH_f, where $\Delta H_f = \mu^{\text{bulk}}_{\text{III-V}} - (\mu^{\text{bulk}}_{\text{III}} + \mu^{\text{bulk}}_{\text{V}})$ is the formation enthalpy of the bulk III-V crystalline phase [29] (note that ΔH_f is intrinsically negative). Eq. (3.1) can then be rewritten to show more clearly the dependence of γ on the surface stoichiometry and chemical potential:

$$\gamma = \gamma_0 + \mu_{\text{V}} \Delta\Theta. \tag{3.2}$$

Here $\gamma_0 = (E_t - E_{\text{sub}}) - \mu^{\text{bulk}}_{\text{III-V}} \Theta_{\text{III}} + \mu^{\text{bulk}}_{\text{V}} \Delta\Theta$ is independent of the chemical potentials, and $\Delta\Theta = \Theta_{\text{III}} - \Theta_{\text{V}} = (n_{\text{III}} - n_{\text{V}})/A$ is the deviation of the surface stoichiometry from its bulk value. The dependence of γ on chemical potential is given entirely by the second term. Note that μ_{V} is intrinsically negative, and can take values in the range $\Delta H_f \leq \mu_{\text{V}} \leq 0$. Hence, Eq. (3.2) reflects in a simple way that III-rich reconstructions ($\Theta_{\text{III}} > \Theta_{\text{V}}$) are favored under III-rich conditions ($\mu_{\text{V}} \rightarrow \Delta H_f$), V-rich reconstructions ($\Theta_{\text{V}} > \Theta_{\text{III}}$) are favored under V-rich conditions ($\mu_{\text{V}} \rightarrow 0$), and for stoichiometric reconstructions ($\Theta_{\text{V}} = \Theta_{\text{III}}$) γ does not depend on chemical potential.

To compute the total-energy contribution, γ_0, to the surface energy we performed first-principles calculations using density-functional theory (DFT). The calculations were performed within the local-density approximation (LDA) [15, 39] using ultrasoft pseudopotentials [49, 52, 87]. We used a standard supercell technique, modeling the (001) surface with a slab consisting of four bilayers and 10 Å of vacuum. Atoms in the bottom bilayer were fixed at their bulk positions, while all other atoms are allowed to relax until

the rms force was less than 0.005 eV/Å. The bottom layer (either Ga or Al) was passivated with pseudohydrogens. A plane-wave cutoff of 300 eV was used, and reciprocal space was sampled with a density equivalent to at least 192 k-points in the (1×1) surface Brillouin zone. To define the III-V formation enthalpy ΔH_f from the bulk chemical potentials μ^{bulk}, separate DFT calculations were performed for the elements in their ground-state phases: Ga in the α-Ga structure, Al in the face-centered cubic structure, Sb in the rhombohedral structure, and both AlSb and GaSb in the zinc blende structure.

3.3 Results and Discussions

The resulting relative surface energies for AlSb(001) and GaSb(001) are shown in Figs. 3.5 and 3.6, respectively, for the eight models considered here. For each model, the surface energy is linear in μ_{V}, with the slope given by $\Delta\Theta$.

For AlSb(001) the predicted stable reconstructions, and their energetic ordering, are in excellent agreement with experiment. Proceeding from Sb-poor to Sb-rich conditions, the predicted sequence is $\alpha(4\times3) \rightarrow \beta(4\times3) \rightarrow \gamma(4\times3) \rightarrow c(4\times4)$, as reported previously [89]. This is the same sequence observed experimentally [89]. Moreover, $\gamma(4\times3)$ is predicted to exist only over a very narrow range of μ_{Sb}, in agreement with experiment [89].

For GaSb(001) the predicted sequence is qualitatively the same as for AlSb(001), although the $c(4\times4)$ is only predicted to be stable for values of μ_{Sb} above the thermodynamically allowed limit of zero. Experimentally, however, the situation is quite different. As reported previously, neither the $\gamma(4\times3)$ nor the $c(4\times4)$ phase is observed for

Table 3.1 Electron count for different reconstructions of the GaSb(001) surface.

Structure	A	n_{III}	n_{V}	Θ_{III}	Θ_{V}	$\Delta\Theta$	$\tilde{n}$	$\tilde{m}$	$\Delta\nu$	$\gamma(\mathrm{Ga}_{rich})$	$\gamma(\mathrm{Sb}_{rich})$
α(4×3)	12	4	4	0.333	0.333	0.0	62	62	0	0.000	0.000
β(4×3)	12	1	7	0.083	0.583	-0.5	68	68	0	0.076	-0.074
γ(4×3)	12	0	8	0.0	0.667	-0.667	70	70	0	0.114	**-0.087**
$h0$(4×3)	12	0	8	0.0	0.667	-0.667	70	70	0	0.118	-0.083
c(4×4)	8	0	6	0.0	0.750	-0.750	50	50	0	0.142	-0.084
c(2×10)	10	0	8	0.0	0.800	-0.800	65	62	0.3	0.255	0.014
(2×10)	20	0	24	0.0	1.200	-1.200	170	164	0.3	0.528	0.166
s1a-c(2×10)	10	1	7	0.1	0.700	-0.600	63	62	0.1	0.143	**-0.038**
s1b-c(2×10)	10	1	7	0.1	0.700	-0.600	63	62	0.1	0.181	0.000
s1c-c(2×10)	10	1	7	0.1	0.700	-0.600	63	62	0.1	0.280	0.099
s2a-c(2×10)	10	2	6	0.2	0.600	-0.400	61	62	-0.1	0.137	0.016
s2b-c(2×10)	10	2	6	0.2	0.600	-0.400	61	62	-0.1	0.124	0.003
s2c-c(2×10)	10	2	6	0.2	0.600	-0.400	61	62	-0.1	0.143	0.023
s2d-c(2×10)	10	2	6	0.2	0.600	-0.400	61	62	-0.1	0.141	0.020
s2e-c(2×10)	10	2	6	0.2	0.600	-0.400	61	62	-0.1	0.167	0.046
s2f-c(2×10)	10	2	6	0.2	0.600	-0.400	61	62	-0.1	0.144	0.023
s2g-c(2×10)	10	2	6	0.2	0.600	-0.400	61	62	-0.1	0.182	0.062
s2h-c(2×10)	10	2	6	0.2	0.600	-0.400	61	62	-0.1	0.164	0.043
s2i-c(2×10)	10	2	6	0.2	0.600	-0.400	61	62	-0.1	0.166	0.045

Note: The excess electron count per (1×1) surface unit cell is defined as $\Delta\nu = (\tilde{n} - \tilde{m})/A$ where $\tilde{n}$ is the number of available electrons and $\tilde{m}$ is the number of required electrons to satisfy the ECM in the excess of Sb-terminated GaSb(001). A is the area of the surface unit cell in terms of the (1×1) surface unit cell. n_i is number of adatoms of species i in excess with respect to the Sb-terminated GaSb(001) and $\Theta_i = n_i/A$ is the coverage of adatoms of species i. The relative γ values, in eV per (1×1) surface unit cell, are given with respect to that of α(4×3).

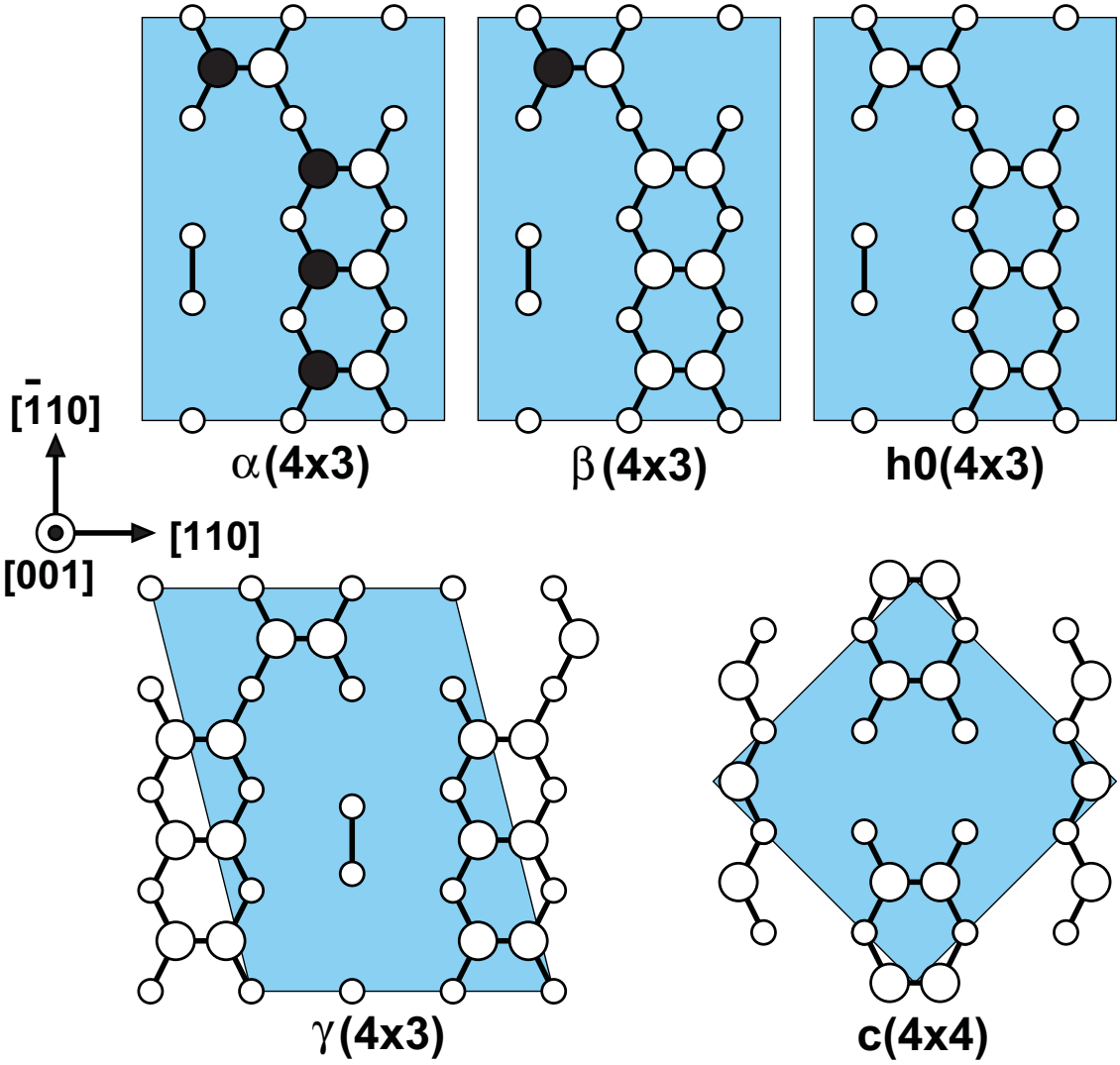

Figure 3.1 Proposed reconstruction models with (4×3) and (4×4) periodicities.

Reconstruction models proposed for the AlSb(001) or GaSb(001) surfaces with (4×3) and (4×4) periodicities. The first two upper layers are shown in a top view. Smaller white circles represent Sb atoms in the top layer of the underlying Sb-terminated AlSb(001) or GaSb(001) surface. Larger circles represent Al or Ga (black) and Sb (white) adatoms. The unit cells are shown in light blue.

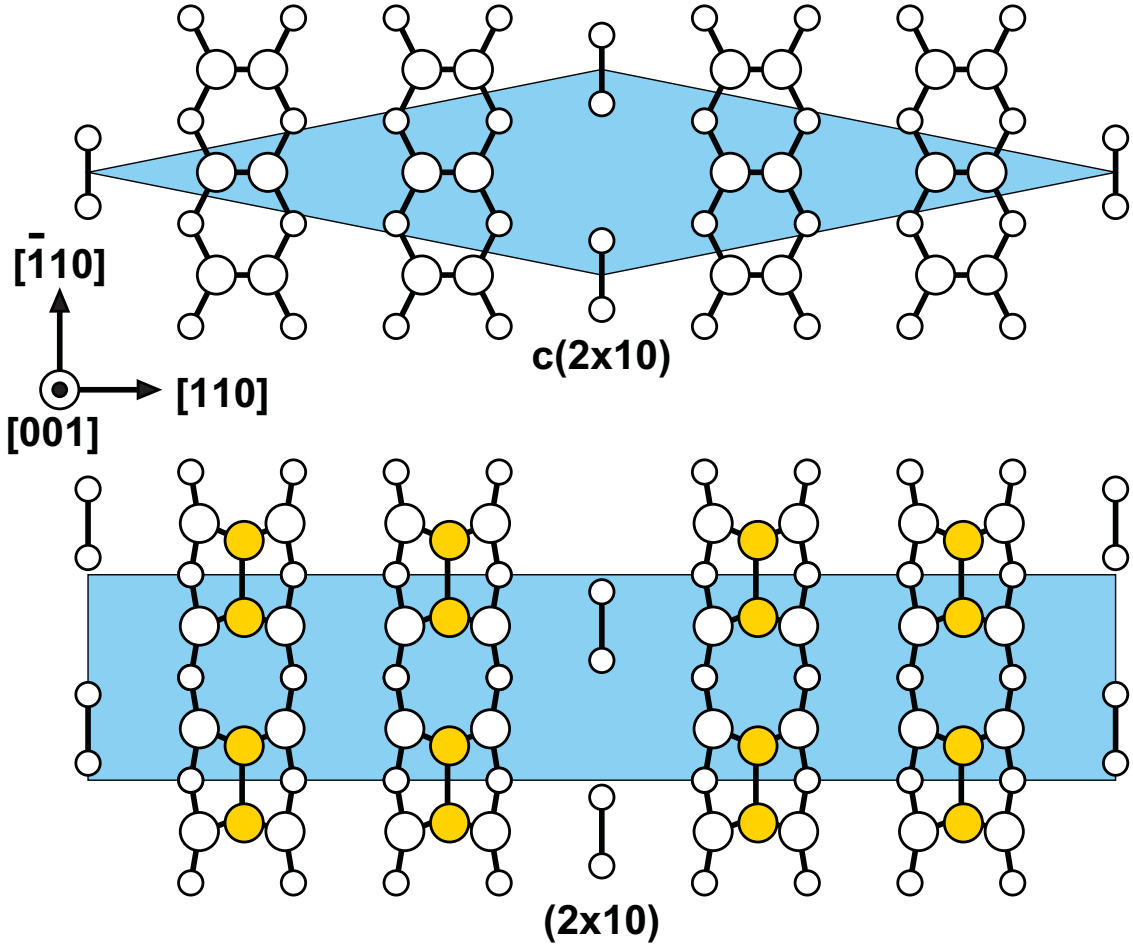

Figure 3.2 Proposed reconstruction models for the GaSb(001)-(1×5)-like surfaces.

See Fig. 3.1 for color schemes. Gold circles represent the second layer Sb adatoms.

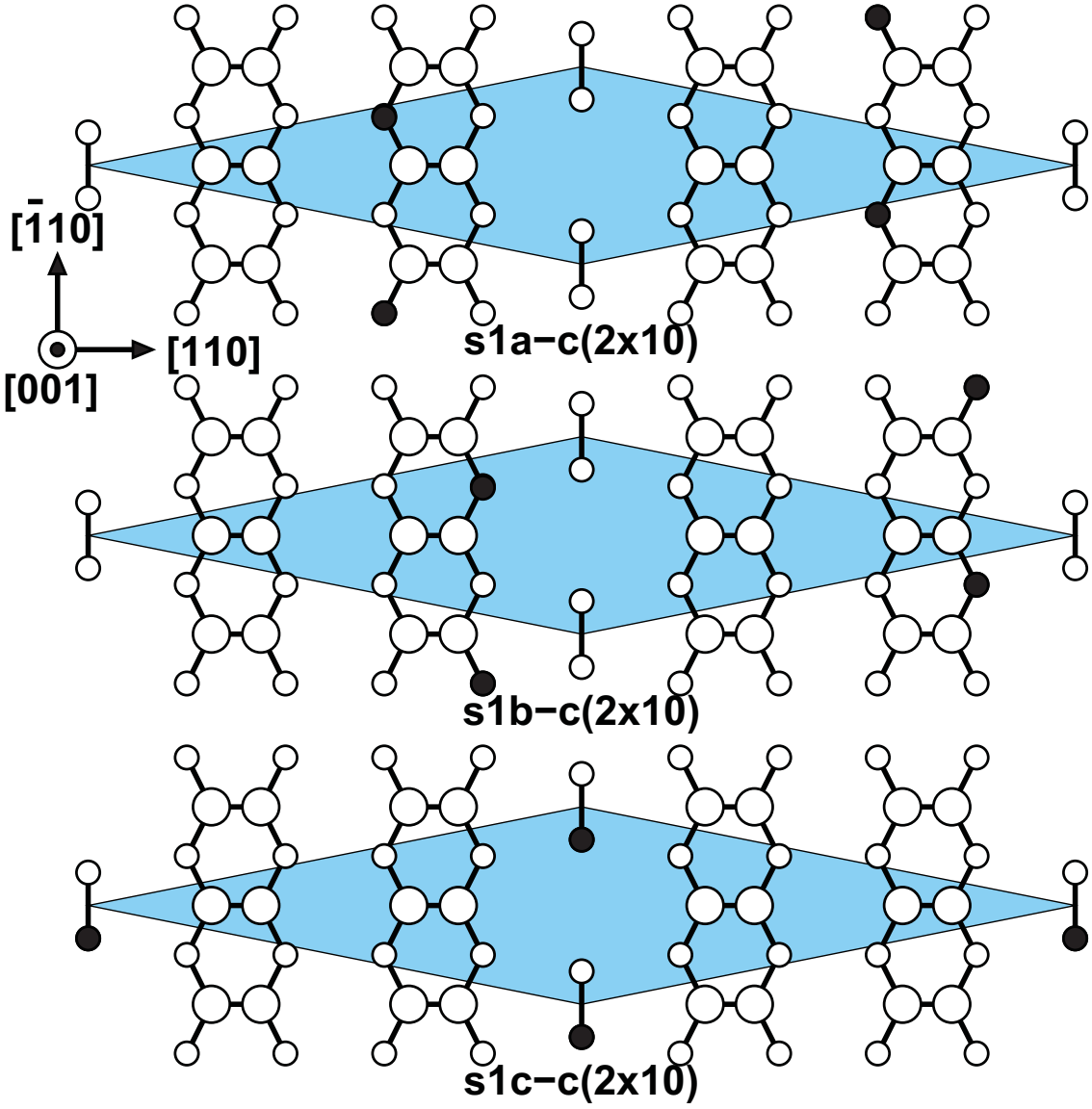

Figure 3.3 Reconstruction models with a single substitution of Sb atoms by Ga atoms.

See Fig. 3.1 for color schemes.

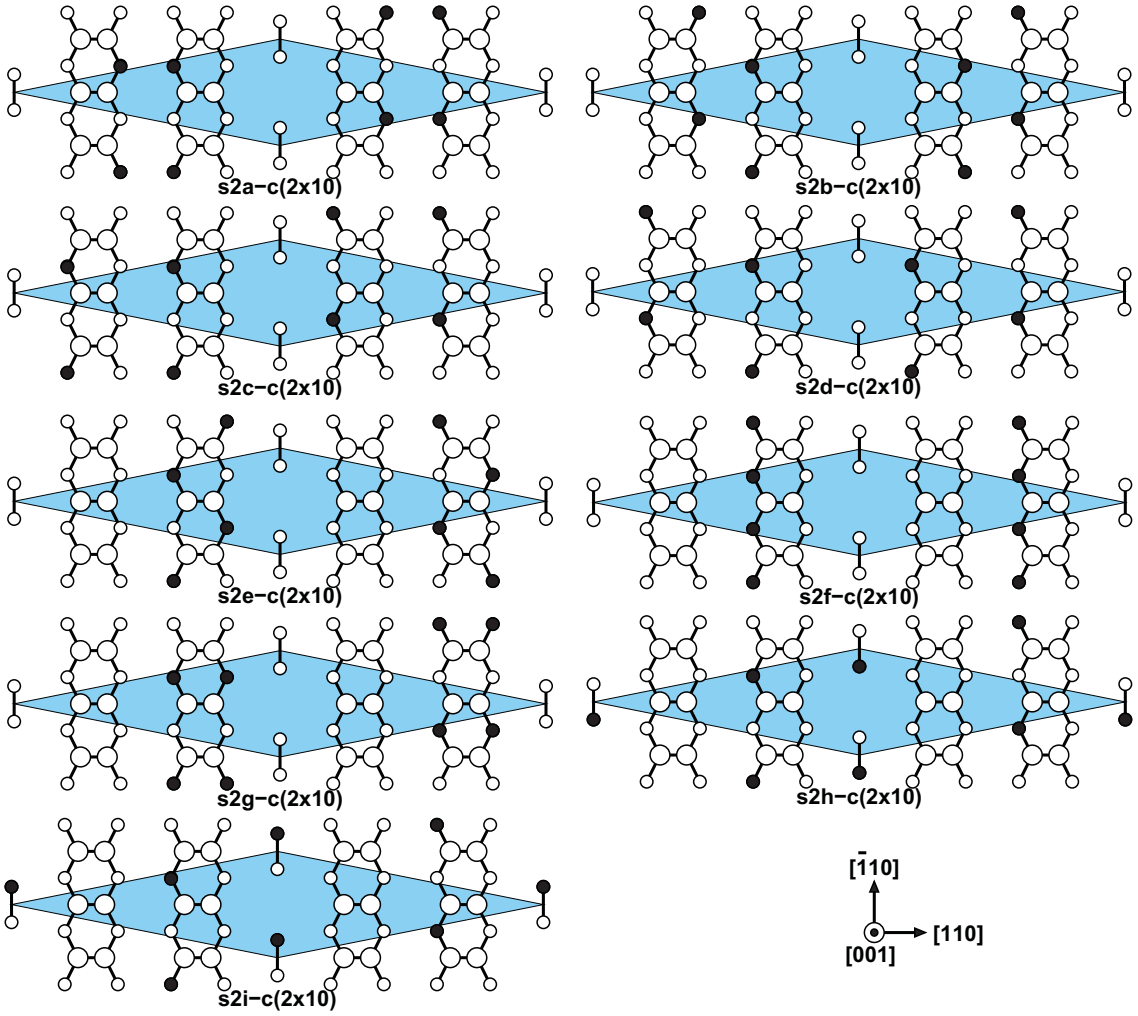

Figure 3.4 Reconstruction models with a double substitution of Sb atoms by Ga atoms.

See Fig. 3.1 for color schemes.

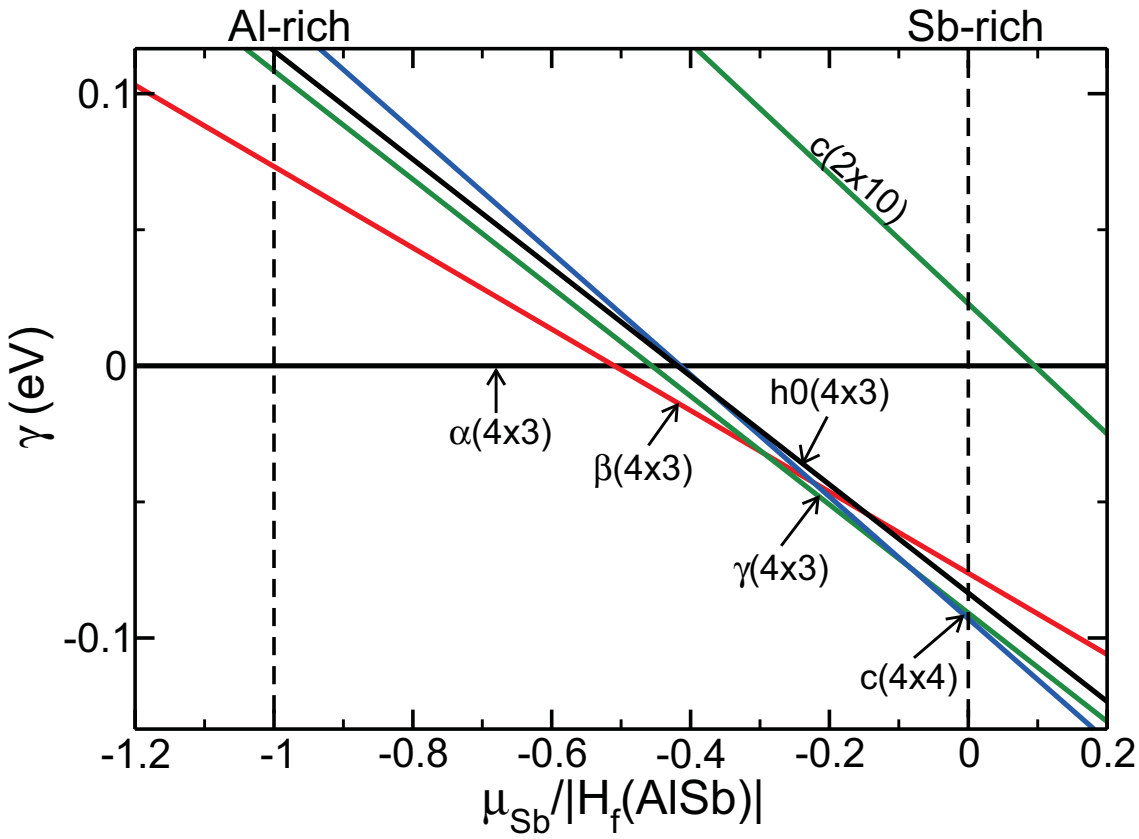

Figure 3.5 Surface stability phase diagram for AlSb(001) surfaces.

The relative surface energy [Eq. (3.2)] is plotted as a function of the Sb chemical potential relative to its corresponding bulk value. Dotted vertical lines mark the thermodynamically allowed range of μ_{Sb}. ΔH_f is the heat of formation for AlSb.

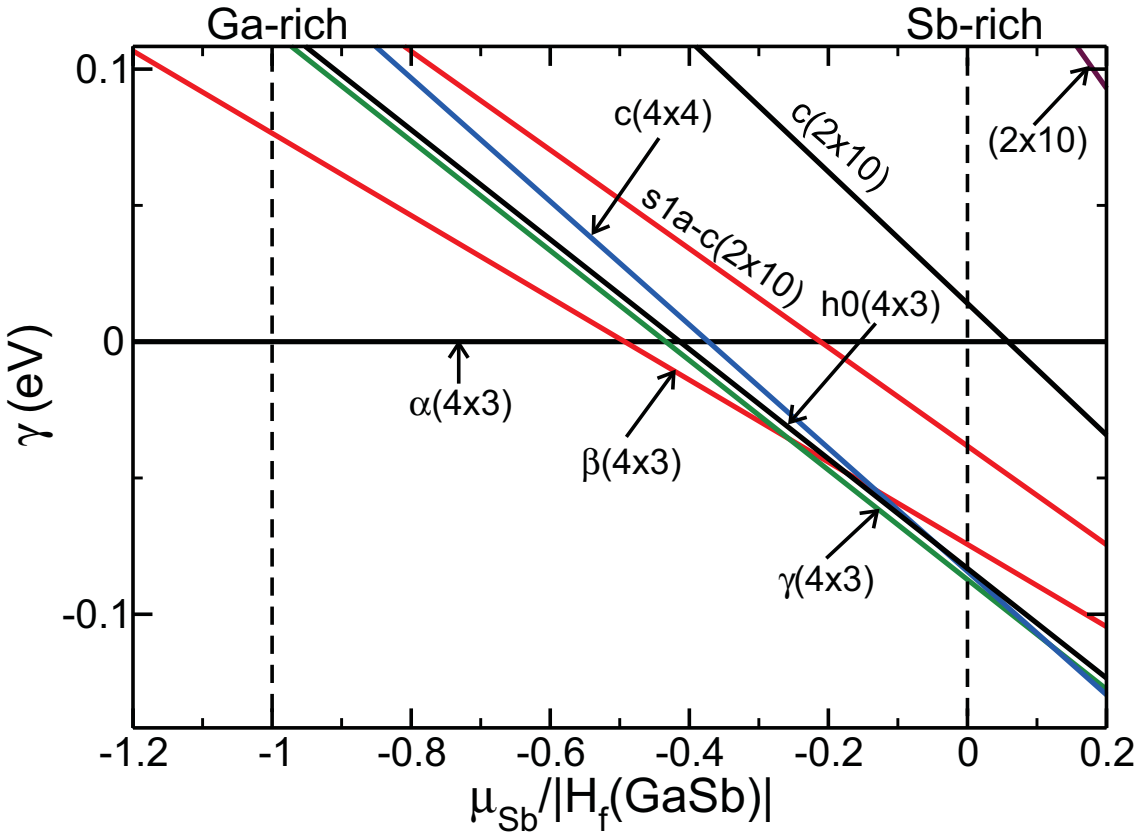

Figure 3.6 Surface stability phase diagram for GaSb(001) surfaces.

The relative surface energy [Eq. (3.2)] is plotted as a function of the Sb chemical potential relative to its corresponding bulk value. Dotted vertical lines mark the thermodynamically allowed range of μ_{Sb}. ΔH_f is the heat of formation for GaSb.

any growth condition [89]. Instead, under Sb-rich conditions, only the (1×5) and (2×5) periodicities have been observed [55].

Righi *et al.* suggested $h0$(4×3), shown in Fig. 3.1, as the model for the GaSb(001) surface under these conditions [61]. Our calculation indeed shows that it is energetically as favorable as γ(4×3), as shown in Fig. 3.6 and in Table 3.1. However, $h0$(4×3) must be rejected as it has a wrong periodicity.

In order to explain the experimentally observed (1×5) and (2×5) structures on the GaSb(001) surface, we studied a large number of structures based on variations of c(2×10) and (2×10). We note that c(2×10) violates the ECM substantially ($\Delta\nu = 0.3$) and substitution of Sb atoms in the top layer of the underlying Sb-terminated GaSb(001) surface by Ga atoms can lower the excess electron count. Fig. 3.3 shows the possible reconstructions when a single Sb atom is replaced by a Ga atom. We use the naming convention of $s1x$ to denote a "single substitution". As shown in Table 3.1, all $s1x$ reconstructions indeed have lower excess electron counts.

For completeness, we also considered reconstructions resulting from double substitution of Sb atoms by Ga atoms as shown in Fig. 3.4. More substitutions, however, were not found to be energetically favorable: Table 3.1 shows that the surface energy of these structures are higher than that of $s1x$ reconstructions. We note that for these double substitutions the excess electron counts $\Delta\nu$ are negative, indicating a deficit of electrons relative to the ECM.

One of the most energetically favorable structures having the correct periodicity is s1a-c(2×10), shown in Fig. 3.3. s1a-c(2×10) has two clear advantages over c(2×10).

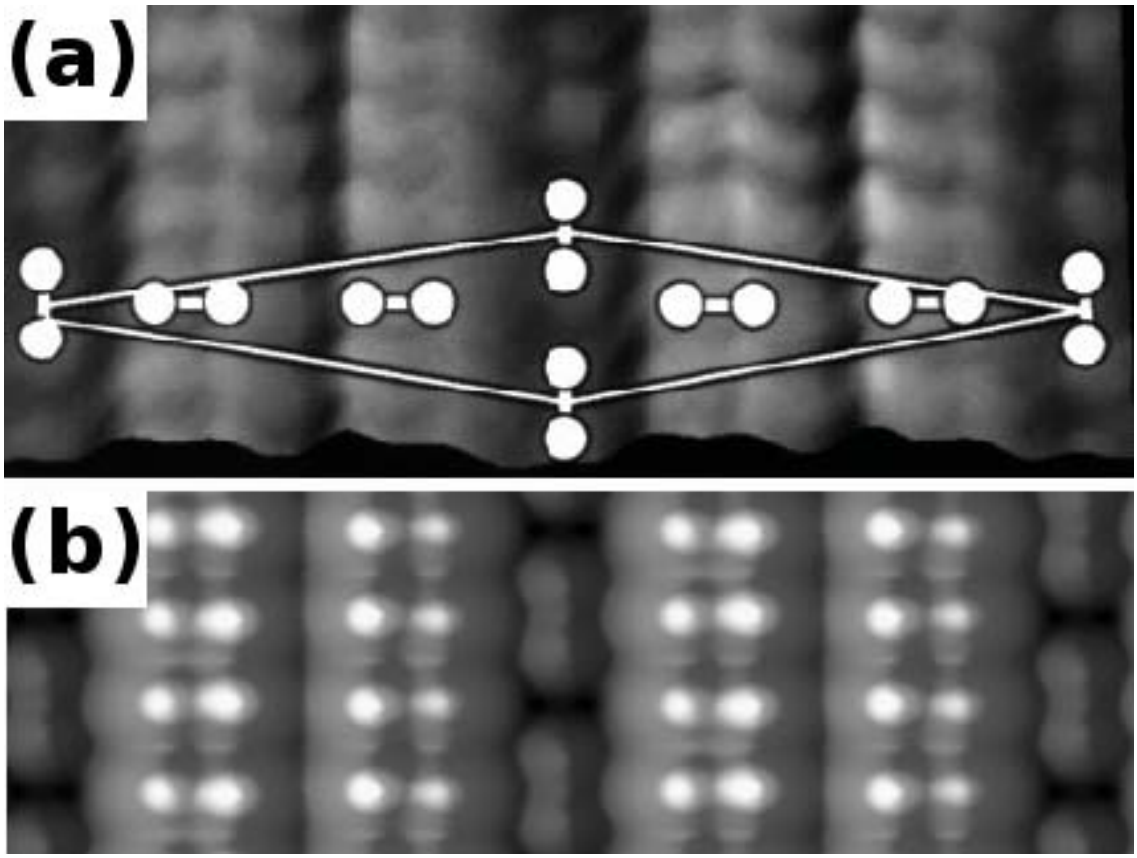

Figure 3.7 Filled-state STM images of GaSb(001) with (1×5) periodicity.

(a) Experimental STM image; a $c(2\times10)$ unit cell is indicated. (b) Simulated STM image of s1a-$c(2\times10)$. This image shows the asymmetries in the intensities of the current density from two atoms of the horizontal dimers, which was not captured in the simulated STM image of $c(2\times10)$. Compare with Fig. 3(d) of Ref. [55].

First, the surface energy for s1a-$c(2\times10)$ is lower than that of $c(2\times10)$ by more than 50 meV per (1×1) unit cell. Second, as shown in Fig. 3.7, the simulated STM image for s1a-$c(2\times10)$ is in a better agreement with the experiment image, in that it reproduces the left-right asymmetry within the surface Sb dimers [55]. Furthermore, as shown in Table 3.1, this model violates the ECM and thus is predicted to be weakly metallic, as observed in tunneling spectroscopy [24]. Therefore, the previously proposed model $c(2\times10)$ is unlikely to be the experimentally realized structure.

However, the calculated surface energy of s1a-$c(2\times10)$ is *higher* than that of $\gamma(4\times3)$, as shown in Table 3.1 and Fig. 3.6. Likewise, (2×10), the structural model generally accepted for the surface with (2×5) periodicity, is the least energetically favorable structure among the eight structures of Table 3.1. On the other hand, $\gamma(4\times3)$, the most energetically favorable structure among all the structures considered in this study, has a periodicity that has not been observed experimentally to date. These facts leave us with two possible conclusions: either the correct structural model remains undiscovered, or the experimentally obtained surface is not the ground-state structure.

The latter possibility, a kinetically limited surface, bears closer consideration. For example, there may be an activation barrier to forming the mixed dimers on GaSb that cannot be overcome within the growth temperatures and times used here. Indeed, to stabilize these surfaces during the growth, one must go from active growth with both Ga and Sb flux at $\sim$500 °C, to room temperature and no flux while trying to stabilize the surface. This process typically involved simultaneously lowering the temperature while turning off the Ga and then lowering the Sb flux. The surface cannot be annealed, because that would

drive off Sb and create ($n\times3$) reconstructions. These considerations lead us to propose that the s1a-c(2×10) structure is the most likely model for the observed GaSb(001) surface as created under Sb-rich growth conditions and subsequently stabilized under vacuum.

3.4 Summary and Conclusions

We have performed *ab initio* calculations on the surface energy and atomic structure of AlSb(001) and GaSb(001) surfaces with various reconstructions. Surface stability diagrams for a large number of reconstruction models are constructed under different growth conditions. For AlSb(001), we confirmed that the predictions of the currently accepted models are in good agreement with experimentally observed reconstructions. For GaSb(001), we showed that previously proposed model accounts for the experimentally observed reconstructions under Ga-rich growth conditions, but fails to explain the experimental observations under Sb-rich conditions. Therefore, we propose s1a-c(2×10) as a better alternative to existing models for GaSb(001) under extreme Sb-rich growth conditions. Our calculations show that s1a-c(2×10) has a substantially lower surface energy than all ($n\times5$)-like reconstructions proposed previously and, in addition, it leads to a simulated STM image in better agreement with experiment than existing models. However, s1a-c(2×10) has higher surface energy than γ(4×3), a model with periodicity that has not been observed. Hence we conclude that the experimentally observed (1×5) and (2×5) structures on GaSb(001) are not the ground-state structure, but kinetically limited ones.

CHAPTER 4

AL-MG-ZN TERNARY Φ PHASE

The crystal structure that was proposed by Bourgeois et al. [10] for the Φ phase of Al-Mg-Zn alloys has been validated and refined using DFT calculations. Their model defined 10 sets of symmetry equivalent sites occupied by either Zn or Al atoms with other sites definitely occupied by Mg atoms. DFT calculations were used to determine optimal Zn and Al locations within the unit cell. The model consists of a total of 84 Mg atoms and 68 Zn/Al atoms, that we resolved to be 84 Mg, 32 Al, and 36 Zn atoms for the most energetically stable configuration. We also show other nearly as stable configurations at other elemental concentrations over the experimentally observed range.

4.1 Introduction

The Φ phase is one of two established ternary phases of Al-Mg-Zn alloys [79]. Bourgeois et al. [10] proposed a crystal structure, and validated it by comparing calculated electron diffraction patterns with experiment. They also established the space group as Pbcm. They could not, however, completely resolve whether some sites were Al or Zn. In this paper we confirm the proposed structure via total energy calculations using the tie line concept.

Mg sites are unambiguously defined in the crystal structure. The proposed structure, however, has 10 sets of symmetry equivalent sites occupied by either Zn or Al. Of those ten sets, one is a 4a, two are 4d, and seven are 8e as described by Wyckoff positions for the space group Pbcm. The Mg atoms are distributed via five 4d and eight 8e sites. The internal parameters and lattice constants of the most stable configuration of the proposed model our listed in Table 4.2. This results in $2^{10} = 1024$ possible structures assuming symmetry related atoms are the same elements, for which DFT calculations were performed.

Using the approximate internal parameters provided by L. Bourguies candidate arrangements were created by exhaustively trying combinations of Zn or Al in the 10 (Al,Zn) sites in the proposed crystal structure. Atomic positions as well as lattice constants were optimized for each configuration.

The Φ phase was first reported by Clark [13] in 1961, which he called γ. He showed the presence of the Φ phase at 40 Mg, 40 Zn, and 20 Al [weight %] or 54.9 Mg, 20.4 Zn, 24.7 Al [atomic %], which falls withing the solubility ranges determined by later studies [20, 58]. The narrow solubility range of Mg in the Φ phase is 53 to 55 at.%, and the Al and Zn contents vary widely from 18 to 29 and from 28 to 17 at.%, respectively [20].

4.2 Computational Method

The first principles calculations were based on Density Functional Theory (DFT) [34, 48]. We used Blöchl's Projector-Augmented Wave (PAW) method [9] potentials as generated by G. Kresse[54] using the Generalized Gradient Approximation (GGA).

We used a 300 eV kinetic energy cutoff. A k-point mesh with 4x2x2 subdivisions using the Monkhorst-Pack scheme [70] was sufficient to converge the total energy. Atomic and volume relaxations were performed. The calculations were restarted two times for each candidate configuration to ensure large volume changes didn't affect the final energies reported, because of a constant number of plane-waves set at the start of calculation.

4.3 Results

The relative stability energy E_{rel} is defined as:

$$E_{rel} = E_{Mg_{84}(Al_x,Zn_{1-x})_{68}} - xE_{Mg_{84}Al_{68}} - (1-x)E_{Mg_{84}Zn_{68}} \tag{4.1}$$

where x is [0,1]. When $x = 0$ all (Al,Zn) atoms are Zn, and $x = 1$ all (Al,Zn) atoms are Al. The energy is zero when $x = 0$ or 1, and negative for energetically favorable structures.

The general parabolic shape of the lowest relative stability energy configurations per each concentration shows that alloying Zn and Al into this crystal structure results in a lowering of the relative stability energy. The red line along the bottom axis refers to the range of Al as a percentage of the (Al,Zn) sites that correspond to what is found experimentally in Φ phase crystals. The extreme cases of $x = 0$, $Mg_{84}Zn_{68}$ and $x = 1$,

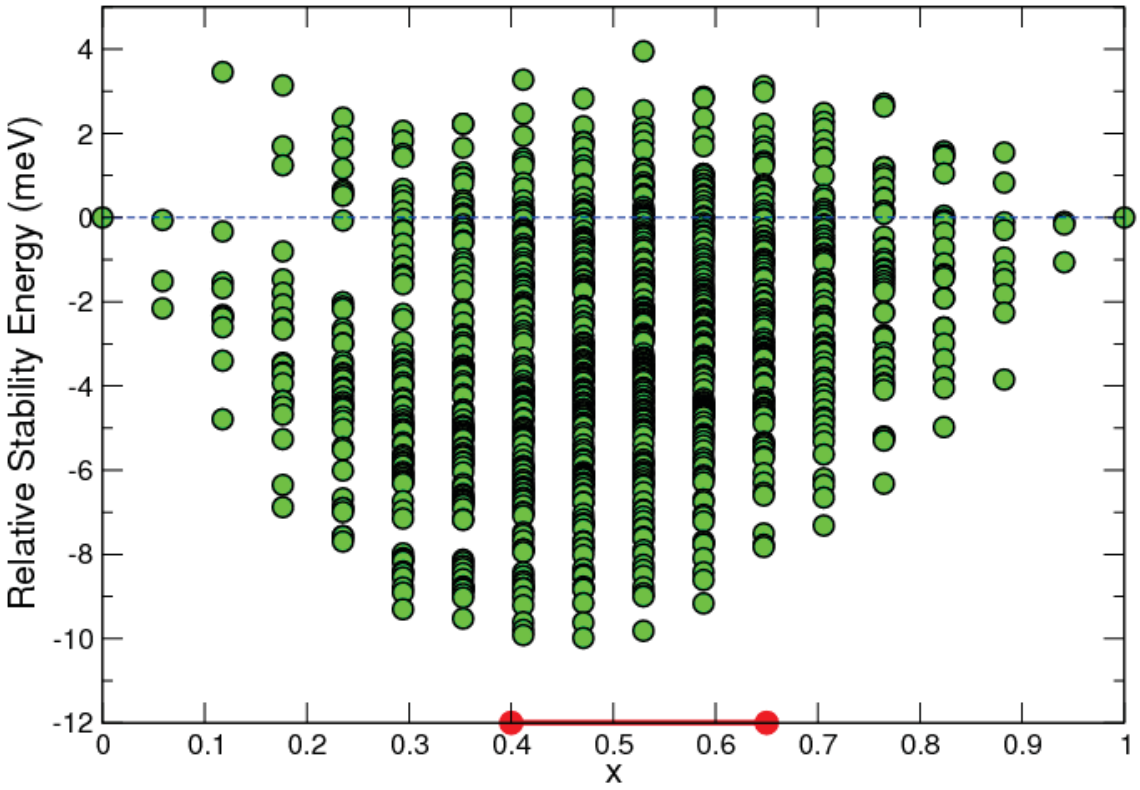

Figure 4.1 Relative Stability of $Mg_{84}(Al_x, Zn_{1\text{-}x})_{68}$ using the tie line concept.

The red line is range of $\frac{Al\%}{Al\%+Zn\%}$ compositions labeled as Φ phase in [58]

.

$Mg_{84}Al_{68}$ are set to zero as reference energies. The rest of the data points are a result of the two extreme cases and the candidate's total energy using Eq. 4.1 to calculate the relative stability energy, because comparing total energy for different concentrations would be erroneous. The discreteness of x values arises from the number of atoms per symmetry related coordinates being either 4 or 8. There is no way without breaking the symmetry of the system to have an even 34 Zn and 34 Al atom for example.

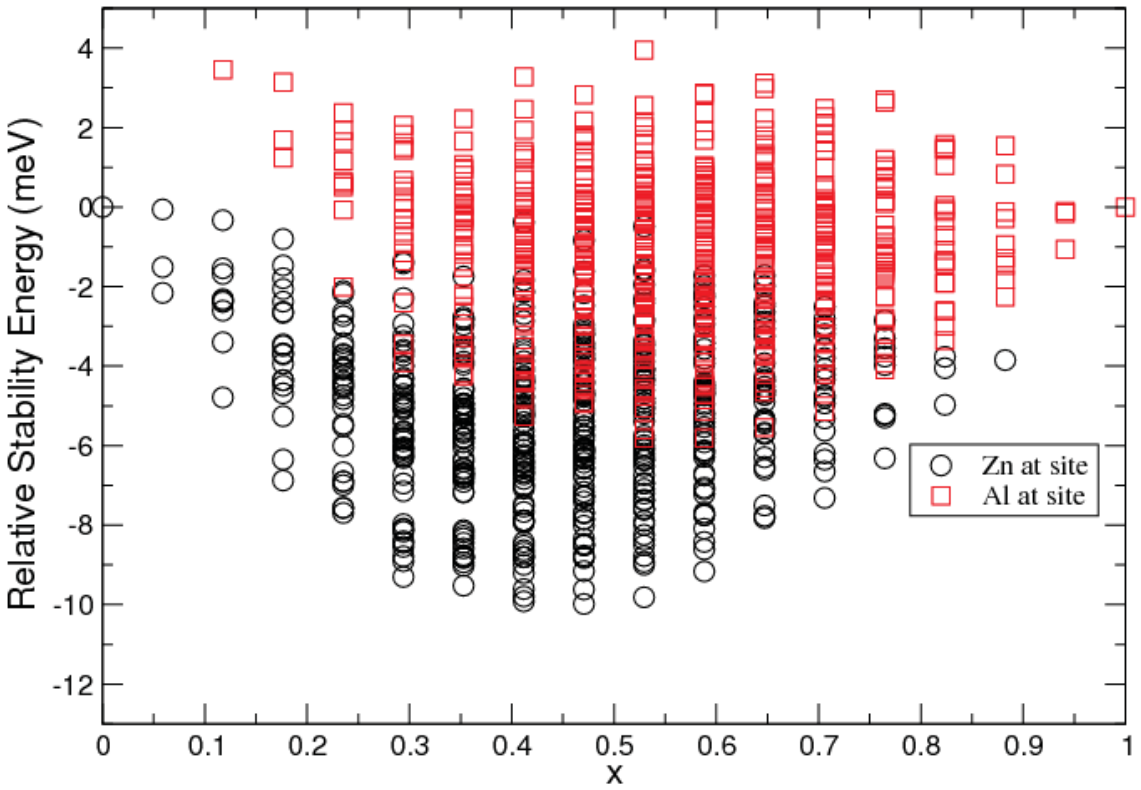

Figure 4.2 Relative stability energy comparing Al or Zn in Site 2.

The lowest energy of the candidates is within the experimental range of Al to Zn determined by [58]. This study was exhaustive under the restriction that symmetry equiv-

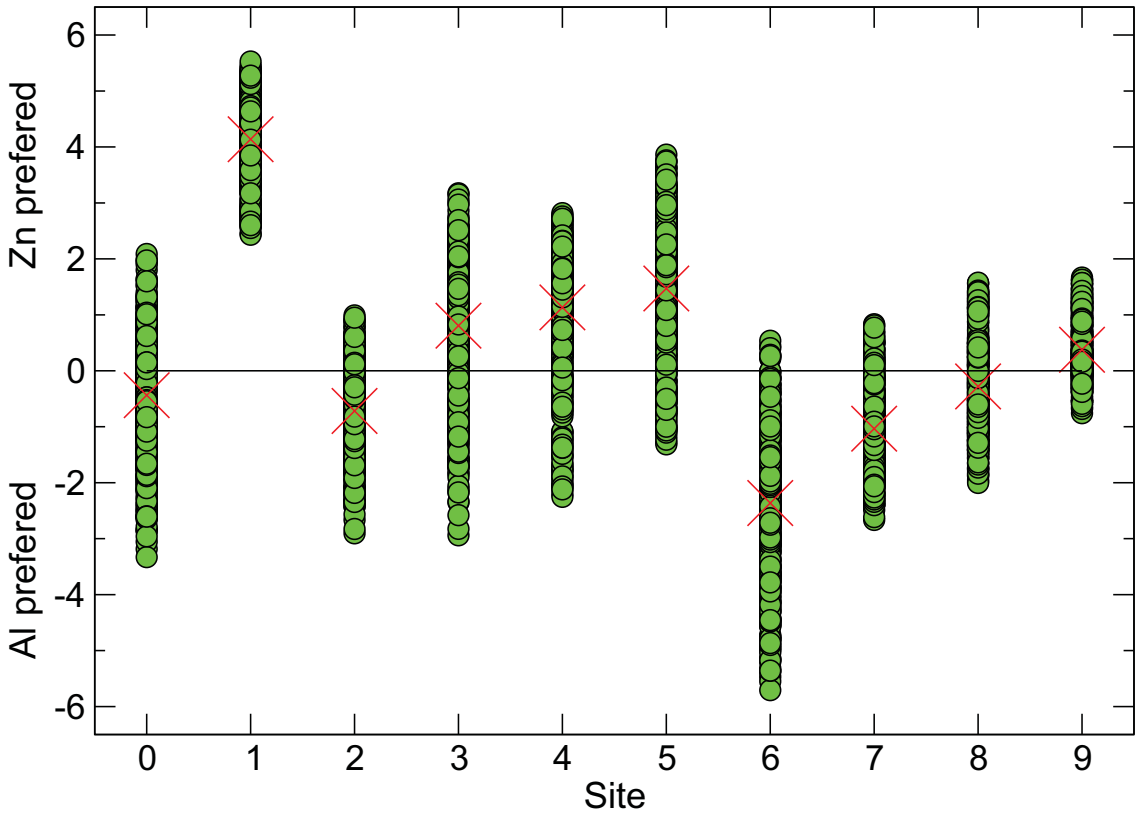

Figure 4.3 Differences in relative stability of listed site being occupied by Al or Zn.

Table 4.1 Statistics of ΔE_{rel} for the 10 (Al,Zn) sites.

Site	Mean	Std. D.	Min	Max	Zn	Al
1	-0.44	0.98	-3.33	2.09	180	332
2	4.14	0.65	2.43	5.53	512	0
3	-0.72	0.70	-2.90	0.99	78	434
4	0.81	1.09	-2.94	3.17	406	106
5	1.13	1.09	-2.25	2.82	435	77
6	1.47	1.17	-1.31	3.86	448	64
7	-2.36	1.30	-5.71	0.54	8	504
8	-1.03	0.77	-2.66	0.83	61	451
9	-0.28	0.85	-2.00	1.57	191	321
10	0.38	0.54	-0.76	1.67	380	132

Note: $\Delta E_{rel} = E_{rel}$(Al at site#) $- E_{rel}$(Zn at site#)

alent positions within the crystal were occupied by the same element. The number of configurations preserving symmetry with 28, 32, and 36 Al atoms are 126, 140, and 140 respectively. While mixed occupancies were not calculated due to the shear number of possible configurations, an analysis of each (Al,Zn) site preference for Al or Zn is presented. Figure 4.2 shows the relative stability energy plot with data points indicating whether site 2 was occupied by Al or Zn. There is a clear trend of Zn occupation lowering the relative stability energy for this site. We calculated the difference of relative stability energies for each (Al,Zn) site being Al and it being Zn with the other nine sites them same. This results in 512 differences being calculated for each site that elucidates any preference for occupation by Zn or Al. The results are plotted in Figure 4.3 and listed in Table 4.1. The average of energies gained or lost when Al or Zn occupies those positions. Positive means Zn and negative means Al occupation lowered the relative stability energy. The standard deviation, minimum , and maximum of the 512 values for each site are given. Finally, the number of configurations that benefited from either Zn or Al occupying the site are tallyed. Site 2 was the only one whose energy was never lowered by having Al instead of Zn. Site 7 had the least number of arrangements when Zn lowered the relative stability energy, but no site showed an absolute preference for Al.

The lattice constants and internal parameters to build the lowest relative stability energy unit cell are given in Table 4.2 for the Al/Zn and Mg sites. Bourgeois et al. [10] reported that the best match of computed diffraction patterns occurred when sites 1-5 and sites 6-10 were occupied by Al and Zn atoms respectively. That data point is $x = 0.412$

Table 4.2 Lattice constants and internal parameters of optimal structure

Atom(site)	symmetry	x	y	z
Al(1)	4a	0.00 (0.00)	0.00 (0.00)	0.00 (0.00)
Zn(2)	4d	0.40 (0.37)	0.69 (0.68)	1/4 (1/4)
Al(3)	4d	0.65 (0.62)	0.60 (0.59)	1/4 (1/4)
Al(4)	8e	0.66 (0.62)	0.46 (0.46)	0.18 (0.18)
Zn(5)	8e	0.41 (0.37)	0.41 (0.42)	0.12 (0.12)
Zn(6)	8e	0.16 (0.14)	0.37 (0.37)	0.18 (0.18)
Zn(7)	8e	0.16 (0.14)	0.51 (0.50)	0.12 (0.12)
Al(8)	8e	0.16 (0.14)	0.64 (0.63)	0.18 (0.18)
Zn(9)	8e	1.00 (0.98)	0.25 (0.25)	0.12 (0.13)
Al(10)	8e	0.91 (0.90)	0.41 (0.41)	0.11 (0.11)
Mg(1)	4d	0.67 (0.68)	0.00 (0.00)	1/4 (1/4)
Mg(2)	4d	0.03 (0.04)	0.00 (0.00)	1/4 (1/4)
Mg(3)	4d	0.46 (0.44)	0.33 (0.32)	1/4 (1/4)
Mg(4)	4d	0.84 (0.83)	0.32 (0.32)	1/4 (1/4)
Mg(5)	4d	0.11 (0.12)	0.21 (0.19)	1/4 (1/4)
Mg(6)	8e	0.45 (0.44)	0.59 (0.59)	0.13 (0.11)
Mg(7)	8e	0.67 (0.65)	0.01 (0.02)	0.52 (0.52)
Mg(8)	8e	0.14 (0.15)	0.09 (0.09)	0.12 (0.12)
Mg(9)	8e	0.84 (0.81)	0.16 (0.16)	0.03 (0.02)
Mg(10)	8e	0.33 (0.35)	0.24 (0.22)	0.13 (0.14)
Mg(11)	8e	0.67 (0.66)	0.28 (0.28)	0.12 (0.13)
Mg(12)	8e	0.16 (0.15)	0.34 (0.34)	0.02 (0.02)
Mg(13)	8e	0.49 (0.48)	0.34 (0.33)	1.00 (0.01)

Note: Lattice constants of optimal configuration a=8.82 (8.98)Å b=16.73 (16.99)Å c=1.971 (19.34)Å. Values in parenthesis are starting values taken from Bourgeois et al.[10] approximate coordinates.

and $E_{rel} = -6.725$ meV. The lowest energy configuration has sites 1, 3, 4, 8, and 10 as Al and sites 2, 5, 6, 7, and 9 as Zn. This result is $x = 0.471$ and $E_{rel} = -10$ meV.

Which element is occupying each of the 10 (Al,Zn) sites in the 10 most energetically favorable crystals can be derived from Figure 4.4. They range from 20 to 40 Al atoms, and up to -0.8 meV difference in related stability energy. Starting with the most favorable configuration containing 32 Al atoms and E_{rel} = -10 meV whose site occupancies are listed the connections indicate which site is changed to arrive at that configuration. Switching site 7, 8 atoms, from Zn to Al will be the lowest configuration with 40 Al and E_{rel} = -9.2 meV. From there switching site 1, 4 atoms, from Al to Zn gets to the most favorable configuration with 36 Al atoms. Besides keeping track of what changed from the lowest configuration any move to the right is Zn to Al and any move to left in figure is Al to Zn. One connection exists in this figure that involves two sites changing elements simultaneously. It involves switching site 2 to Al which was already shown to never prefer Al, but simultaneously changing site 3 to Zn keeps the Al content at 28 atoms and costs 0.7 meV.

4.4 Conclusion

We explored the possible combination of Al-Mg-Zn in the proposed crystal structure. We Determined minimum energy configurations using DFT energy calculations. The minimum energy structure occurs in the range of experimentally observed atomic concentrations, which confirms the model correctly describes the Φ phase crystal structure.

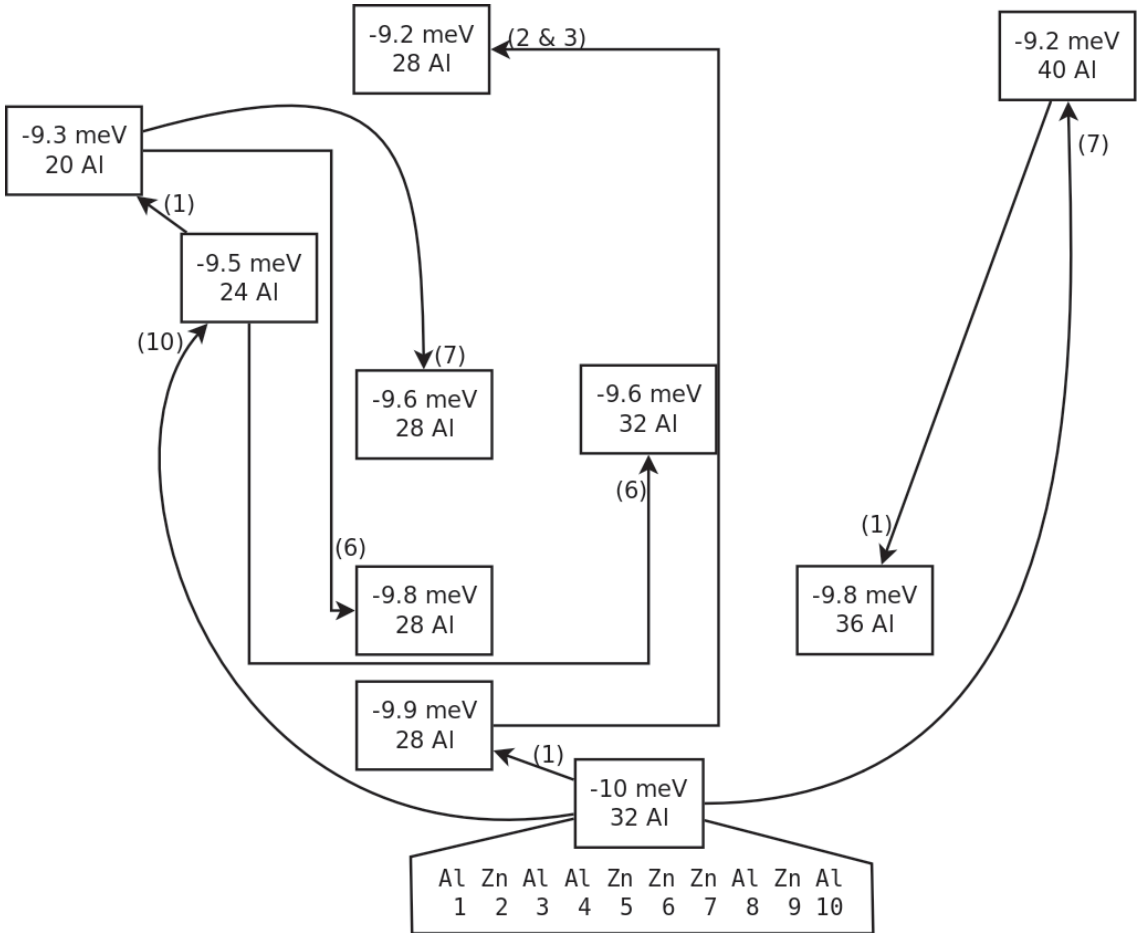

Figure 4.4 Connections to lowest energy configuration.

The value in parenthesis is the site that differs between the connected configurations.

CHAPTER 5

STEEL

5.1 Introduction

Iron is known to be a ferromagnetic material with a body center cubic crystal structure. DFT can predict this as the correct ground state as shown in 5.1. The generalized gradient approximation must be used along with doing a spin-polarized calculation to include the energy from magnetism. The PAW method gives a better agreement with the more accurate all electron methods. For the rest of the chapter involving Fe calculations the PAW-GGA potential is used.

Table 5.1 Bulk Fe energies for different potentials, phases, and magnetic setting.

	PAW-LDA	PAW-GGA	USPP-LDA	USPP-GGA
bcc Fe FM	151	-66	87	-238
bcc Fe NM	431	387	430	383
fcc Fe NM	87	79	86	76
hcp Fe NM	0	0	0	0

Note: For the four potential and exchange-correlation type combinations the non-magnetic hcp is the reference value.

The Fe-C phase diagram, figure 5.1, illustrates the temperature ranges and solubility of carbon in the Ferrite and Austenite Phases. The right most part of the phase diagram

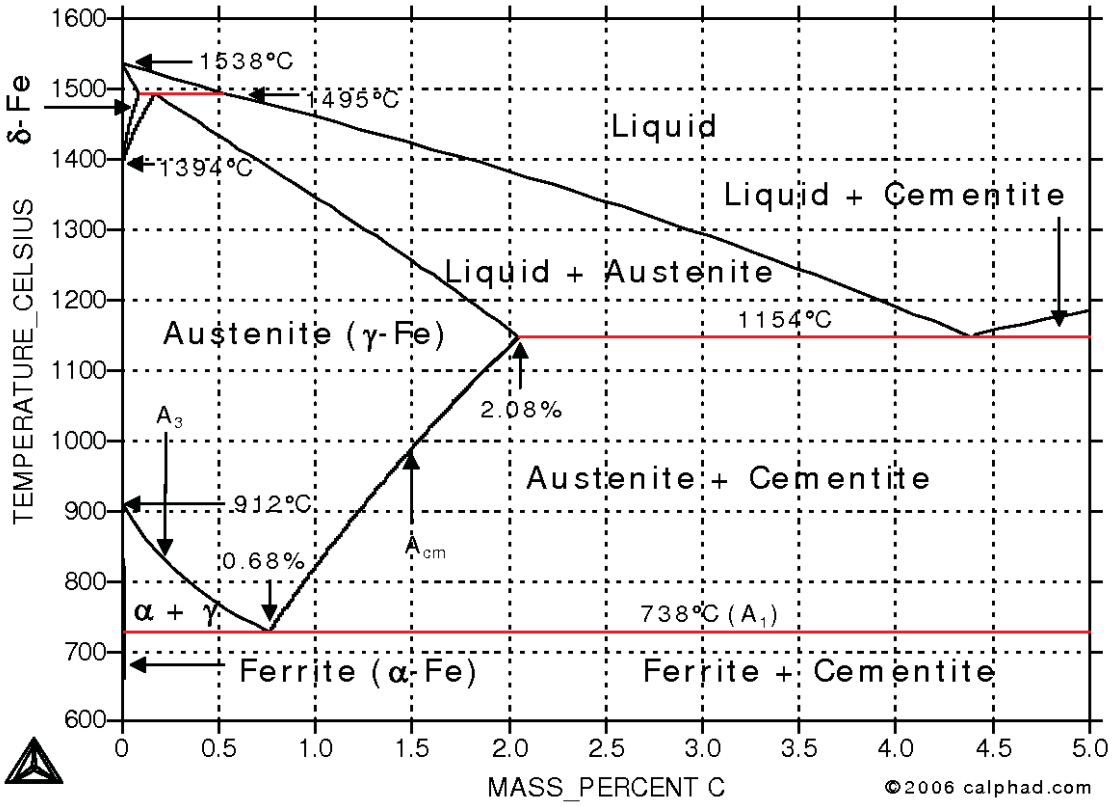

Figure 5.1 Fe-C phase diagram

is Cementite. The carbon concentration regions in the middle are mixtures of the compound Cementite and pure Fe phases. The diagram only represents what can be formed based on Fe and Carbon content. Heat treatment of the Fe-C system can effect the microstructure of the steel. Slow cooling of Austenite with carbon results in the formation of Pearlite, planes of Cementite between regions of Ferrite. Rapid cooling prevents the Carbon from diffusing and the formation of Cementite. The result is a supersaturated and unstable structure called Martensite.

Cementite (Fe_3C) is a metastable compound with an orthorhombic crystal structure. The unit cell contains four iron atoms in symmetry related Fe(I) positions, eight more iron atoms at Fe(II) positions, and four symmetric carbon atoms. Table 5.2 give the formulas for relating the atomic positions in the Cementite unit cell, and table 5.3 gives the values commonly called internal parameters for the locations of the atoms.

Table 5.2 Cementite unit cell structure.

Atom	Basis vectors (a_0**x**, b_0**y**, c_0**z**)
C	$(x_1, \frac{1}{4}, z_1)$,$(-x_1, \frac{3}{4}, -z_1)$,$(\frac{1}{2} - x_1, \frac{3}{4}, \frac{1}{2} + z_1)$,$(\frac{1}{2} + x_1, \frac{1}{4}, \frac{1}{2} - z_1)$
Fe(I)	$(x_2, \frac{1}{4}, z_2)$,$(-x_2, \frac{3}{4}, -z_2)$,$(\frac{1}{2} - x_2, \frac{3}{4}, \frac{1}{2} + z_2)$,$(\frac{1}{2} + x_2, \frac{1}{4}, \frac{1}{2} - z_2)$
Fe(II)	(x_3, y_3, z_3),$(-x_3, -y_3, -z_3)$,$(\frac{1}{2} + x_3, \frac{1}{2} - y_3, \frac{1}{2} - z_3)$,$(\frac{1}{2} - x_3, \frac{1}{2} + y_3, \frac{1}{2} + z_3)$, $(-x_3, \frac{1}{2} + y_3, -z_3)$,$(x_3, \frac{1}{2} - y_3, z_3)$,$(\frac{1}{2} - x_3, -y_3, \frac{1}{2} + z_3)$,$(\frac{1}{2} + x_3, y_3, \frac{1}{2} - z_3)$

Table 5.3 Internal parameters of Cementite.

	a_0	b_0	c_0	x1	z1	x2	z2	x3	y3	z3
Exp	5.09	6.74	4.53	0.890	0.450	0.036	0.850	0.186	0.063	0.328
DFT	5.03	6.72	4.47	0.876	0.438	0.035	0.837	0.176	0.068	0.332

5.2 Point Defect Energies In Cementite

The crystal structure of Cementite is illustrated in Figure 5.2 with a Vanadium atom substituted at an Fe lattice site. Point defect energies for vacancies and substitutional defects are listed in Table 5.4. Vacancy formation energy is given by

$$E_{\text{vacancy}} = E_{\text{tot}}[\text{Vac}] - E_{\text{tot}}[\text{Cementite}] + \varepsilon \tag{5.1}$$

where $E_{\text{tot}}[\text{Vac}]$ is the total energy of the system with an atom missing at the indicated site, $E_{\text{tot}}[\text{Cementite}]$ is the total energy of Cementite without a defect, and ε is the energy per atom in its most stable bulk structure. Substitutional defect energy is given by

$$E_{\text{sub}} = E_{\text{tot}}[\text{Defect}] - E_{\text{tot}}[\text{Cementite}] + \varepsilon[\text{replaced}] - \varepsilon[\text{added}] \tag{5.2}$$

where $E_{\text{tot}}[\text{Defect}]$ is the total energy of the system with the point defect, $\varepsilon[\text{added}]$ and $\varepsilon[\text{replaced}]$ are energies per atom for the element that is occupying and what should by occupying the site respectively. Again these ε values are from the most stable bulk structure calculated in independent runs. A vacancy or Carbon substitutional defect in an Fe(II) site

is slightly less costly than an Fe(I) site. A Vanadium substitutional defect in Cementite for Fe is energetically favorable, and slightly more so in Fe(II) sites than Fe(I) sites.

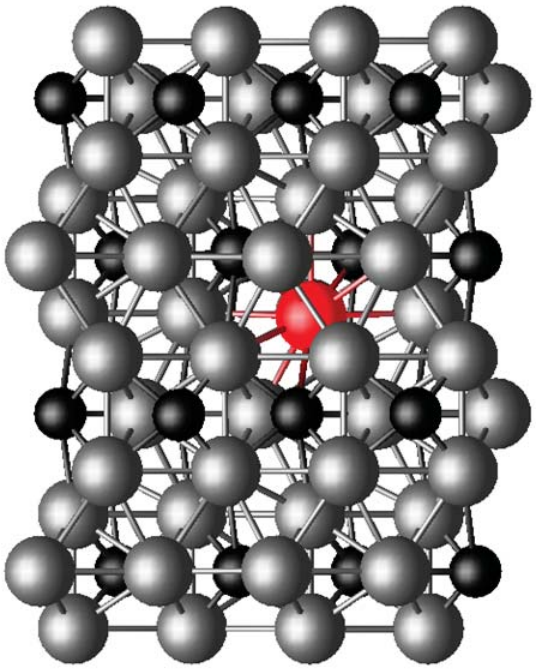

Figure 5.2 Vanadium substitution in Cementite.

5.3 Diffusion Barrier Calculations

For simple point defect calculations in Cementite it doesn't matter which of the eight Fe(II), four Fe(I), or four C, is removed as in a vacancy calculation or substituted because they are equivalent. Fe(I) atoms have two Fe(I), ten Fe(II), and two C neighbors. Fe(II) atoms have five Fe(I), six Fe(II), and three C neighbors. The two Fe(I) neighbors of an Fe(I) atom are identical for computing diffusion barriers. Additionally the ten Fe(II) neighbors of an Fe(I) atom are composed of five pairs of identical paths. Finally we are

Table 5.4 Defect formation energies in Cementite (eV)

$E_{\text{Vacancy}}[\text{Fe(I)}]$	1.56
$E_{\text{Vacancy}}[\text{Fe(II)}]$	1.40
$E_{\text{Vacancy}}[\text{C}]$	0.56
$E_{\text{Sub}}[\text{C} \rightarrow \text{Fe(I)}]$	3.01
$E_{\text{Sub}}[\text{C} \rightarrow \text{Fe(II)}]$	2.82
$E_{\text{Sub}}[\text{Fe} \rightarrow \text{C}]$	2.21
$E_{\text{Sub}}[\text{V} \rightarrow \text{Fe(I)}]$	-0.61
$E_{\text{Sub}}[\text{V} \rightarrow \text{Fe(II)}]$	-0.72
$E_{\text{Sub}}[\text{V} \rightarrow \text{C}]$	1.77

Note: $E_{\text{Sub}}[\text{A} \rightarrow \text{B}]$ means that an atom of element A is occupying site B.

interested in diffusion from an Fe(II) to Fe(II) site of which the six neighbors reduce to four paths.

The diffusion barrier calculations were performed using the nudged elastic band (NEB) method with a climbing image [31]. NEB is a method for finding minimum energy paths between two known configurations. In our calculation that would be fully relaxed monovacancies at neighboring sites. We used ten intermediate structures or images for our calculations. The method finds lowest energy configurations while maintaining equal spacing to neighboring images. This total spacing or displacements between images is the reaction coordinate value plotted in figure 5.3. The climbing image modifies the NEB method so that one image is located at the saddle point and the spacing to either side is maintained, but most likely will be different to the left and right of the saddle point.

The diffusion barriers calculated in Figure 5.3 were calculated in a large unitcell consisting of 8 primitive Cementite unitcells. For this case Fe atoms 1-32 are in Fe(I) positions Fe atoms 33-96 are in Fe(II) positions.

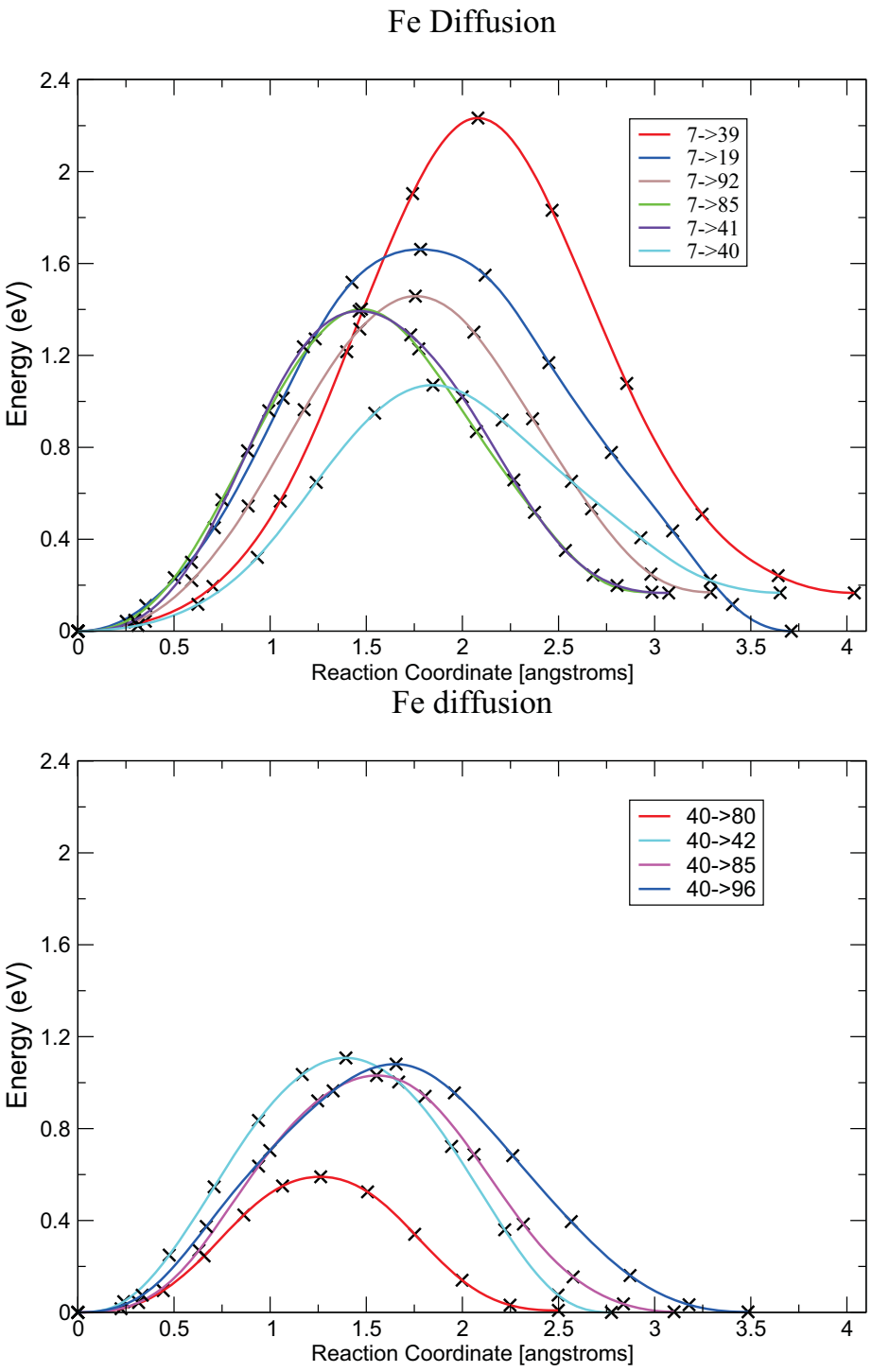

Figure 5.3 Fe diffusion in Cementite.

Diffusion of Fe from an Fe(I) site in Cementite, and diffusion of Fe from an Fe(II) site.

Looking at the the first plot in Figure 5.3 only the 7 to 19 path i.e. the single Fe(I) to Fe(I) path returns back to the same energy. While these figures illustrates the ten diffusion paths of Fe in Cementite, five of the paths are not symmetric involving diffusing from or to an Fe(I) and an Fe(II) site. The barrier to overcome is lower going from the Fe(II) than from Fe(I) sites. Values are presented in Tables 5.5 and 5.6 depending on the site to be filled.

Table 5.5 Diffusion into Fe(I) site of Fe(7) in Cementite

Path 1	Path 2	Path 3	Path 4	Path 5	Path 6
2.07	1.66	1.29	1.23	1.23	0.90

Path 1: from Fe(39) or Fe(79). Path 2: from Fe(19) or Fe(23).
Path 3: from Fe(52) or Fe(92). Path 4: from Fe(63) or Fe(85).
Path 5: from Fe(41) or Fe(67). Path 6: from Fe(40) or Fe(80).

Table 5.6 Diffusion into Fe(II) site of Fe(40) in Cementite

Path 1	Path 2	Path 3	Path 4	Path 5	Path 6	Path 7	Path 8	Path 9
2.23	1.46	1.40	1.39	1.11	1.08	1.07	1.03	0.59

Path 1: from Fe(8). Path 2: from Fe(24). Path 3: from Fe(30). Path 4: from Fe(10).
Path 5: from Fe(42). Path 6: from Fe(92) or Fe(96). Path 7: from Fe(7).
Path 8: from Fe(85) or Fe(86). Path 9: from Fe(80)

CHAPTER 6

MEAM OPTIMIZATION

Semi-empirical potential methods including the embedded-atom method (EAM) and the modified embedded-atom method (MEAM) are reviewed. The procedures to construct these potentials are also reviewed. A multi-objective optimization (MOO) procedure has been developed to construct modified-embedded-atom-method (MEAM) potentials with minimal manual fitting. This procedure has been applied successfully to develop a new MEAM potential for magnesium. The MOO procedure is designed to optimally reproduce multiple target values that consist of important material properties obtained from experiments and first-principles calculations based on density-functional theory (DFT). The optimized target quantities include elastic constants, cohesive energies, surface energies, vacancy formation energies, and the forces on atoms in a variety of structures. The accuracy of the new potential is assessed by computing several material properties of Mg and comparing them with those obtained from other potentials previously published. We found that the present MEAM potential yields a significantly better overall agreement with DFT calculations and experiments.

6.1 Introduction

Molecular dynamics simulations are effective tools used to study many interesting phenomena such as the melting and coalescence of nanoparticles at the atomic scale [46, 82]. These atomistic simulations require accurate interaction potentials to compute the total energy of the system, and first-principles calculations can provide the most reliable interatomic potentials. However, realistic molecular dynamics simulations often require an impractical number of atoms that either demands too much computer memory or takes too long to be completed in a reasonable amount of time. One alternative is to use empirical or semi-empirical interaction potentials that can be evaluated efficiently.

Additionally, there are two essential features that are expected from a useful semi-empirical approach besides its efficiency: reliability and flexibility. A reliable interatomic potential would accurately reproduce various fundamental physical properties of the relevant element or alloy, such as elastic, structural, and thermal properties. Reliability also includes transferability. A transferable interatomic potential would perform reasonably well even under circumstances that were not used during its construction phase. A flexible semi-empirical approach can represent interaction potentials among a wide variety of elements and their alloys using a common mathematical formalism.

Despite its remarkable successes, one of the most notable difficulties in using MEAM, as well as any of the alternative modern potentials, is that the construction of the MEAM potentials involves a lot of manual and *ad hoc* fittings. Because of the complex relationship between the sixteen MEAM parameters and the resultant behavior of a MEAM potential, a traditional procedure for constructing a MEAM potential involves

a two-step iterative process. First, a *single* crystal structure, designated as the reference structure, is chosen and the MEAM parameters are fitted to construct a MEAM potential that reproduces a handful of critical material properties of the element in the reference structure. Second, the new potential is tested for its accuracy and transferability by applying it to atoms under circumstances not used during its construction phase. These systems include different crystal structures, surfaces, stacking faults, and point defects. If the validation is not satisfactory, one needs to go back to the first step and adjust the parameters in a way that improves the overall quality of the potential. Although this iterative method does work eventually in many cases, it is very tedious and time-consuming. Ercolessi and Adams [22] overcame this shortcoming for EAM potentials by developing a force-matching method that fits the EAM potential to *ab initio* atomic forces of many atomic configurations including surfaces, clusters, liquids and crystals at finite temperature. Later, the force-matching method was extended to include many other material properties such as cohesive energy, lattice constants, stacking fault energies, and elastic constants [57, 59]. Furthermore, several different MEAM potentials for the same element often develop and an objective and quantitative method to measure the relative quality of each potential would be helpful for the researchers who want to choose one of these potentials.

In this work, we extend the force-matching method to develop a multi-objective optimization (MOO) procedure to construct MEAM potentials. Most realistic optimization problems, particularly in engineering, require the simultaneous optimization of more than one objective function. For example, aircraft design, which requires simultaneous

optimization of fuel efficiency, payload and weight, which calls for a MOO procedure. In most cases, it is unlikely that the different objectives would be optimized by the same parameter choices. Therefore, some trade-off between the objectives is needed to ensure a satisfactory design. Stadler [88] introduced the concept of Pareto [75] optimality to the fields of engineering and science. The most widely used method for multi-objective optimization is the weighted sum (utility function) method. A comprehensive overview and comparison of different MOO methods can be found in Ref. [2].

The composite objective function also provides an unbiased measure to quantify the relative quality of different MEAM potentials. We apply the procedure to develop a new MEAM potential for magnesium. The new Mg MEAM potential will be compared with previously published Mg potentials. We chose Mg because of its increased importance in many technological areas, including the aerospace and automotive industries. Due to the lower mass densities of magnesium alloys compared with steel and aluminum and higher temperature capabilities and improved crash-worthiness than plastics, the use of magnesium die castings is increasing rapidly in the automotive industry [30, 77].

Empirical potentials for Mg have been previously proposed by several groups. In 1988, Oh and Johnson [74] developed analytical EAM potentials for hcp metals such as Mg. Igarashi, Kanta and Vitek [38] (IKV) also developed interatomic potentials for eight hcp metals including Mg using the Finnis–Sinclair type many-body potentials, which are a specific form of an EAM potential [26]. Pasianot and Savino [76] proposed improved EAM potentials for Mg based on IKV's fitting scheme. Baskes and Johnson [5] have extended the MEAM to hcp crystal structures. Later, Jelinek et al [42] improved this

potential as a part of the MEAM potentials for Mg-Al alloy system. Liu et al [59] used the force-matching method to develop an EAM potential for Mg.

6.1.1 Multi-objective Optimization

A generic multi-objective optimization (MOO) problem can be formulated as [45, 85]:

$$\begin{aligned} &\min \mathbf{J}(\mathbf{x}) \quad \text{s.t.} \quad x \in S \\ &\text{where } \mathbf{J} = [J_1(\mathbf{x}) \cdots J_m(\mathbf{x})]^T \\ &\mathbf{x} = [x_1 \cdots x_n]^T \end{aligned} \tag{6.1}$$

Here, $\mathbf{J}$ is a column vector of m objectives. The individual objectives are dependent on a vector $\mathbf{x}$ of n design variables in the feasible domain S. The design variables are assumed to be continuous and vary independently. Typically, the feasible design domain is defined by the design constraints and the bounds on the design variables. Ideally, the goal is to minimize all elements of the objective vector simultaneously. However, when the objectives are in conflict, a compromise solution on the Pareto frontier is sought. The most widely used method for MOO is scalarization using the weighted sum method. The method transforms the multiple objectives into an aggregated scalar objective function J that is the sum of each objective function J_i multiplied by a positive weighting factor w_i:

$$J(\mathbf{x}) = \sum_{i=1}^{m} w_i J_i(\mathbf{x}). \tag{6.2}$$

The weighting factors in Eq. (6.2) can be adjusted to increase (or decrease) the influence of a more (or less) important objective in the compromise solution.

In this work, the overall goal is to develop a MEAM potential for Mg. The individual objective functions are constructed from the normalized differences between the MEAM-generated values and the target values similar to that in the global criterion method:

$$J_i(\mathbf{x}) = \left[\frac{Q_i(\mathbf{x}) - Q_i^0}{Q_i^*}\right]^2. \tag{6.3}$$

Here, Q_i is the physical quantity computed using the current MEAM potential parameters and Q_i^0 is the target value to reproduce. The target values are usually experimental values, but the computed values from the first-principles method are chosen when the experimental data are not available. The normalization factor Q_i^* is a typical value for the given material parameter and often $Q_i^* = Q_i^0$. The overall objective function $J(\mathbf{x})$ can be minimized using usual multi-dimensional unconstrained optimization routines. We used the *downhill simplex method* [78] that requires only function evaluations, not derivatives, which require substantially more complicated mathematical expressions and coding.

6.2 Potential Construction Procedure

We used the MOO procedure to develop a new set of MEAM parameters (treated as design variables in Eq. (6.1)) that improves the overall agreement of MEAM results with experiments or *ab initio* calculations. Our previously published MEAM parameters for Mg [42] served as the basis for the present work.

All *ab initio* total-energy calculations and geometry optimizations are performed within density functional theory (DFT) using ultrasoft pseudopotentials (USPP) [87] as implemented by Kresse and his co-workers [50, 53]. For the treatment of electron exchange and correlation, we use the local-density approximation (LDA) [15, 39]. The Kohn-Sham equations are solved using a preconditioned band-by-band conjugate-gradient (CG) minimization [51]. The plane-wave cutoff energy is set to at least 300 eV in all calculations. Geometry relaxations are performed until the energy difference between two successive ionic optimizations is less than 0.001 eV. The Brillouin zone is sampled using the Monkhorst-Pack scheme [71] and a Fermi-level smearing of 0.2 eV was applied using the Methfessel-Paxton method [67].

The objectives used in this work include equilibrium hcp lattice constants a and c at 0 K, the cohesive energy, elastic constants, vacancy formation energy, surface energies, stacking fault energies, and adsorption energies. We also used the forces on Mg atoms in structures equilibriated at six different temperatures. Tables 6.1–6.4 show the complete list of objectives optimized to construct the MEAM potential parameters for Mg and their weights. Weights are chosen to produce a potential that is suitable for general purpose MD simulations. We note that the particular choice presented in this work is indeed somewhat subjective and can be adjusted depending on particular purposes of the simulations. For example, if a very accurate stacking fault energies are desired, the weights for objectives 14–17 in Table 6.3 should be increased. The optimal MEAM parameters (design variables) obtained from the MOO procedure are listed in Table 6.5.

6.2.1 Cohesive Energies

The cohesive energy of Mg atom is defined as the heat of formation per atom when Mg atoms are assembled into a crystal structure:

$$E_{\text{coh}} = -\left(\frac{E_{\text{tot}} - NE_{\text{atom}}}{N}\right), \tag{6.4}$$

where E_{tot} is the total energy of the system, N is the number of Mg atoms in the system, and E_{atom} is the total energy of an isolated Mg atom. The cohesive energies of Mg atoms in hcp, fcc, and bcc crystal structures for several atomic volumes near the equilibrium atomic volumes were calculated. Fig. 6.1 is an example of the cohesive energy plot of Mg atoms as a function of the lattice constant. The minimum of this curve determines the equilibrium lattice constant a_0 and equilibrium cohesive energies $E_{\text{coh}} = E_{\text{hcp}}$ in Table 6.1.

Table 6.1 Bulk properties optimized to construct the MEAM potential.

	Objective	Unit	Weight	Expt	DFT	MEAM[1]	Jelinek[2]	Liu[3]
1	a_0	Å	1.0	3.21 [21]	3.128	3.21	3.21	3.21
2	c/a	–	1.0	1.623 [21]	1.623	1.622	1.623	1.623
3	$E_{\text{coh}} = E_{\text{hcp}}$	eV	2.0	1.51 [47]	1.78	1.51	1.55	1.52
4	B	kbar	1.0	369 [83]	–	376	353	367
5	$E_{\text{fcc}} - E_{\text{hcp}}$	meV	0.72	–	14 [1]	4	4	15
6	$E_{\text{bcc}} - E_{\text{hcp}}$	meV	0.72	–	29 [1]	34	30	18

Note: The parameters for Mg along with the target values and their weights. Comparisons to other Mg potentials are also made. E_{coh} is the cohesive energy, and B is the bulk modulus. The underlined quantities are the target values chosen for the MOO procedure.
[1]MEAM potential from the present work
[2]MEAM potential from Ref. [42]
[3]EAM potential from Ref. [59]

6.2.2 Elastic Constants

Hexagonal crystals have five independent elastic constants: C_{11}, C_{12}, C_{13}, C_{33}, and C_{44} [56]. The elastic constants are calculated numerically by applying small strains to the lattice. For small deformations, the relationship between deformation strain and elastic energy increase in an hcp crystal is quadratic [59]:

1. $\Delta U = \delta^2(C_{11} + C_{12})$, for deformation $x' = x + \delta \cdot x$, $y' = y + \delta \cdot y$,
2. $\Delta U = \delta^2(C_{11} - C_{12})$, for deformation $x' = x + \delta \cdot x$, $y' = y - \delta \cdot y$,
3. $\Delta U = \delta^2 C_{33}/2$, for deformation $z' = z + \delta \cdot z$,
4. $\Delta U = \delta^2(2C_{11} + C_{33} + 2C_{12} + 4C_{13})/2$, for deformation $x' = x + \delta \cdot x$, $y' = y + \delta \cdot y$, $z' = z + \delta \cdot z$,
5. $\Delta U = \delta^2 C_{44}/2$, for deformation $z' = z + \delta \cdot x$,

where unprimed (primed) are the coordinates of the lattice before (after) deformation. ΔU is the elastic energy per volume due to the deformation, and δ is the small strain applied to the lattice. We follow the procedure described by Mehl et al [65] and apply several different strains ranging from -2.0% to $+2.0\%$. The elastic constants are obtained by fitting the resultant curves to quadratic functions. We found that this method gives much more stable results than using one strain value [59]. Table 6.2 shows the result of the MOO procedure for MEAM potential parameters for Mg.

6.2.3 Surface Formation Energies

Surface formation energy per unit surface area is defined as

$$\gamma = \left(E_{\text{tot}} - N\varepsilon\right)/A, \tag{6.5}$$

Table 6.2 Elastic constants comparison of optimized MEAM potential.

	Objective	Unit	Weight	Expt	MEAM[1]	Jelinek[2]	Liu[3]
7	C_{11}	kbar	1.0	635 [83]	606	602	618
8	C_{12}	kbar	1.0	260 [83]	274	237	259
9	C_{13}	kbar	1.0	217 [83]	250	219	219
10	C_{33}	kbar	1.0	665 [83]	631	623	675
11	C_{44}	kbar	1.0	184 [83]	151	155	182

Note: The elastic constants optimized to construct the MEAM potential parameters for Mg along with the target values and their weights. Comparisons to other Mg potentials are also made. The underlined quantities are the target values chosen for the MOO procedure.
[1]MEAM potential from the present work
[2]MEAM potential from Ref. [42]
[3]EAM potential from Ref. [59]

where E_{tot} is the total energy of the system with a surface, N is the number of atoms in the system, ε is the total energy per atom in the bulk, and A is the surface area. Table 6.3 lists the surface formation energies used in this study. The $(10\bar{1}0)$ surface of hcp crystals can be terminated in two ways, either with a short first interlayer distance d_{12} ("short termination") or with a long d_{12} ("long termination") (See, for example, Fig. 2 of Ref. [32]). In this study, we only included the results for the short terminated surface, since it is known to be energetically more favorable over the long terminated surface [84] in agreement with experimental observations in Be$(10\bar{1}0)$ and other hcp metals [32]. Table 6.3 shows surface formation energies optimized to construct the MEAM potential parameters for Mg and the result of the MOO procedure. We notice that the MOO procedure relaxed the level of agreement on these quantities in order to achieve a better overall agreement between reproduced values and target values.

Table 6.3 2-D and 1-D defect formation energies.

	Objective	Unit	Weight	Expt	DFT	MEAM[1]	Jelinek[2]	Liu[3]	Hu[4]
12	$\gamma[(0001)]$	mJ/m^2	1.0	680 [86]	637	583	595	495	310
13	$\gamma[(10\bar{1}0)]$	mJ/m^2	1.0	–	721	625	645	–	–
14	$E_{\text{sf}}[I_1]$	mJ/m^2	0.1	–	18	8	7	27	4
15	$E_{\text{sf}}[I_2]$	mJ/m^2	0.1	–	37	15	15	54	8
16	$E_{\text{sf}}[T_2]$	mJ/m^2	0.1	–	45	15	15	–	–
17	$E_{\text{sf}}[E]$	mJ/m^2	0.1	–	61	23	22	–	12
18	E_{vac}	eV	1.0	0.58–0.89	0.82	0.58	0.56	0.87	0.59

Note: The objectives related to surface formation energies, stacking fault energies and vacancy formation energy optimized to construct the MEAM potential parameters for Mg along with the target values and their weights. γ is the surface energy and E_{sf} is the stacking fault formation energy. Comparisons to other Mg potentials are also made. The underlined quantities are the target values chosen for the MOO procedure.
[1]MEAM potential from the present work
[2]MEAM potential from Ref. [42]
[3]EAM potential from Ref. [59]
[4]Analytic MEAM potential from Ref. [37]

6.2.4 Stacking Fault Energies

Stacking fault formation energy per unit area is defined by

$$E_{\text{sf}} = \left(E_{\text{tot}} - N\varepsilon\right)/A, \tag{6.6}$$

where E_{tot} is the total energy of the structure with a stacking fault, N is the number of atoms in the system, ε is the total energy per atom in the bulk, and A is the unit cell area that is perpendicular to the stacking fault. For Mg, four stacking fault types from the calculation of Chetty et al [12] were examined. The sequences of the atomic layers within the unit cell of our simulations are: $I_1 = ABABABCBCBCB$, $I_2 = ABABABCACACB$, $T_2 = ABABABCBABAB$, and $E = ABABABCABABAB$. We note that the unit

cells for I_1 and I_2 contain *two* stacking faults and the quantities obtained from Eq. (6.6) must be divided by two to obtain the correct formation energies.

6.2.5 Vacancy Formation Energies

The formation energy of a single vacancy E_{vac} is defined as the energy cost to create a vacancy:

$$E_{\text{vac}} = E_{\text{tot}}[N] - N\varepsilon, \tag{6.7}$$

where $E_{\text{tot}}[N]$ is the total energy of a system with N atoms containing a vacancy, and ε is the energy per atom in the bulk. Table 6.3 shows the vacancy formation energy optimized to construct the MEAM potential parameters for Mg.

6.2.6 Atomic Forces

For forces, the objective functions are defined as:

$$J_i(\mathbf{x}) = \frac{(\langle\langle(\mathbf{F} - \mathbf{F}^0)^2\rangle\rangle)^{1/2}}{(\langle\langle(\mathbf{F}^0)^2\rangle\rangle)^{1/2}}, \tag{6.8}$$

where $\mathbf{F}$ are the force vectors on atoms calculated using the MEAM while $\mathbf{F}^0$ are the force vectors from DFT method. $(\langle\langle(\mathbf{F}^0)^2\rangle\rangle)^{1/2}$ represents the root-mean-square of the DFT force, and $(\langle\langle(\mathbf{F} - \mathbf{F}^0)^2\rangle\rangle)^{1/2}$ is the root-mean-square of the error in the force.

To obtain the force data, initial atomic structures that contain 180 Mg atoms were created from the bulk hcp crystal structure. The positions of atoms are randomly disturbed from their equilibrium positions and $10\,000$ steps of molecular-dynamics (MD) simula-

tions with a timestep of Δt = 2.5 ps were performed to equilibrate each structure for different temperatures. In each MD run, we the used Mg MEAM potential by Jelinek [42]. If no MEAM potential were available for MD simulations, one could use an intermediate MEAM potential that is generated with this MOO procedure without the force data. The potential should be adequate enough to obtain a reasonable set of structures. There is a significant issue that one must address in using DFT forces to improve forces of the MEAM potentials. As seen in Table 6.1, DFT predicts a smaller atomic volume or lattice constant than experimentally observed values. Since our MEAM potential is designed to reproduce the experimental lattice constant (objective 1 in Table 6.1), there should be an inherent difference between MEAM- and DFT-generated forces. This difference in interatomic distances makes the direct comparison of *ab initio* and MEAM-predicted forces inaccurate. Following the procedure introduced by Mishin et al [68], we scaled the atom positions by the ratio of the DFT/MEAM lattice constants before we perform DFT calculations to obtain *ab initio* forces used in Table 6.4.

6.3 Results and Discussion

The hcp structure was chosen as the reference structure for Mg. The final MEAM parameters obtained from the MOO procedure are listed in Table 6.5.

6.3.1 Material Properties

Tables 6.1–6.4 list various material properties of Mg selected as the objectives to be optimized in constructing the Mg MEAM potential, along with experimental data

Table 6.4 Force based optimizations

	Objective	Unit	Weight	Expt	DFT	MEAM[1]	Jelinek[2]	Liu[3]	Hu[4]
19	$\Delta\mathbf{F}$ (100 K)	%	1.0	–	<u>0.0</u>	41.98	167.71	–	–
20	$\Delta\mathbf{F}$ (300 K)	%	1.0	–	<u>0.0</u>	35.89	77.82	–	–
21	$\Delta\mathbf{F}$ (500 K)	%	1.0	–	<u>0.0</u>	31.45	126.98	–	–
22	$\Delta\mathbf{F}$ (800 K)	%	1.0	–	<u>0.0</u>	29.77	83.89	–	–
23	$\Delta\mathbf{F}$ (1000 K)	%	1.0	–	<u>0.0</u>	27.76	71.96	–	–
24	$\Delta\mathbf{F}$ (1200 K)	%	1.0	–	<u>0.0</u>	28.12	69.15	–	–

Note: The relative errors in force vectors that were optimized to construct the MEAM potential parameters for Mg. Comparisons to other Mg potentials are also made. The underlined quantities are the target values chosen for the MOO procedure.
[1]MEAM potential from the present work
[2]MEAM potential from Ref. [42]
[3]EAM potential from Ref. [59]
[4]Analytic MEAM potential from Ref. [37]

Table 6.5 Optimized set of MEAM potential parameters for Mg.

E^0[eV]	a_0[Å]	A	α	$\beta^{(0)}$	$\beta^{(1)}$	$\beta^{(2)}$	$\beta^{(3)}$
$t^{(0)}$	$t^{(1)}$	$t^{(2)}$	$t^{(3)}$	C_{max}	C_{min}	r_c	Δr
1.51	3.20	1.14	5.69	2.66	-0.003	0.348	3.32
1.00	8.07	4.16	-2.02	3.22	1.10	5.0	0.353

Note: See the text for the definition of these parameters and their usage. The hcp structure was chosen as the reference structure for Mg.

and *ab initio* data. It also shows how well each objective has been optimized. Results from other previously published Mg potentials are also listed in the table for comparison. Tables 6.1–6.4 also show the weight of individual objectives w_i chosen to optimize the present potential. The underlined quantities are the target values chosen for the MOO procedure. Whenever possible, the experimental values are chosen as the target values. If the experimental values are not available or known to be unreliable, the computed values from the first-principles method are used.

The present MEAM potential reproduces the experimental lattice constant, the c/a ratio, and the cohesive energy near perfectly. Fig. 6.1 shows the cohesive energies of Mg atoms in hcp crystal structure compared with those obtained from the Rose universal equation of state [80] based on the experimental lattice constant, cohesive energy and bulk modulus. It shows a good agreement between the two sets of data. We also note that the sequence of the structures is predicted correctly in the order of stability by the present Mg MEAM potential as shown in Table 6.1.

The surface formation energies of the two common low-index surfaces of hcp Mg crystals are in good agreement with the experimental values, representing a significant improvement over the MEAM potentials by Liu et al [59] or Hu and others [36].

As pointed out by Liu et al [59], the stacking fault energies are difficult quantities for an emprirical potential to reproduce because they only depend on long range interactions beyond second nearest-neighbor distances in hcp crystals. The present MEAM potential shows a substantial improvement over the previously published MEAM potential by Hu et al [37]. The stacking fault energies are consistently underestimated by the

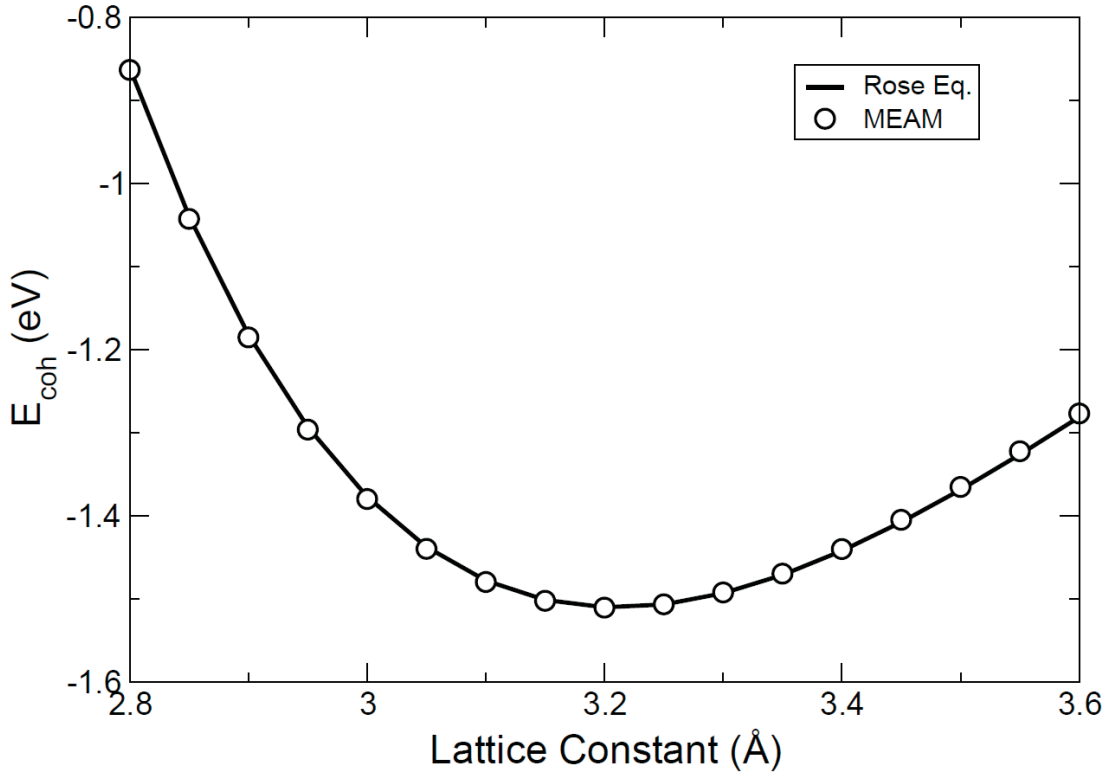

Figure 6.1 Cohesive energies computed from potential compared to Rose eq.

The cohesive energies as a function of the lattice constant a for Mg atoms in hcp crystal structure compared with the ones obtained from the Rose equation. The data points are computed with the present MEAM potential while the curve is obtained from the Rose equation.

present MEAM potential compared to the results of the DFT calculations, while the results by the EAM potential from Ref. [59] are consistently overestimated. Table 6.3 also shows that the formation energy of single vacancies from DFT calculation is reproduced quite reasonably by the present MEAM potential.

Table 6.4 shows the force-matching against the *ab initio*-generated forces. It shows that the MEAM potential from the present work reproduces significantly more accurate forces on atoms compared to the previous MEAM potential [42].

6.3.2 Additional Material Properties

Table 6.6 Unoptimized material properties of the Mg potential.

Property	DFT	MEAM[1]	Jelinek[2]
$E_{\text{ads}}[(000\bar{1})]$	-0.81	-1.46	-1.50
$E_{\text{ads}}[(10\bar{1}0)]$	-1.21	-1.52	-1.56
$E_{\text{f}}^{\text{int}}$ (octahedral)	2.36	1.20	1.29
$E_{\text{f}}^{\text{int}}$ (tetrahedral)	2.35	1.41	1.53

Note: The additional material properties of Mg that are not used as objectives for the construction of the potential. Comparisons are made to other Mg potentials and experiments. E_{ads} is the adsorption energy; $E_{\text{f}}^{\text{int}}$ is the formation energies of interstitial point defects. All energy values are given in eV.
[1]MEAM potential from the present work
[2]MEAM potential from Ref. [42]

To validate the present MEAM potential further, we calculated a few additional material properties of Mg that were not used as objectives during the construction of the

potential. We obtained the adsorption energies of a single Mg atom on different surfaces and the formation energies of interstitial defects as listed in Table 6.6.

The adsorption energy of a single adatom E_{ads} is given by

$$E_{\text{ads}} = E_{\text{tot}} - E_{\text{surf}} - E_{\text{atom}} \tag{6.9}$$

where E_{tot} is the total energy of the structure with the adatom adsorbed on the surface, E_{surf} is the total energy of the surface without the adatom, and E_{atom} is the total energy of an isolated atom. On both (0001) and $(10\bar{1}0)$ surfaces, we placed a single Mg atom at the site where the atoms of the next layer would normally sit. The structures were then relaxed to determine the adsorption energies. Table 6.6 shows that the adsorption energies on two Mg surfaces are quite well reproduced by the present MEAM potential. The present Mg potential gives slightly better adsorption energies than the previously published MEAM potential [42].

The formation energy of an interstitial point defect $E_{\text{f}}^{\text{int}}$ is given by

$$E_{\text{f}}^{\text{int}} = E_{\text{tot}}[N+1] - (E_{\text{tot}}[N] + \varepsilon) \tag{6.10}$$

where $E_{\text{tot}}[N]$ is the total energy of a system with N Mg atoms, $E_{\text{tot}}[N+1]$ is the total energy of a system with N atoms plus one Mg atom inserted at one of the interstitial sites, and ε is the total energy per Mg atom in its most stable bulk structure. Interstitial atom formation energies were calculated for Mg at octahedral and tetrahedral sites. Atomic position and volume relaxation were performed. The results of these calculations are listed

in Table 6.6, to be compared with the results from the DFT calculations. The present MEAM potential predicts correct signs for these energies although the magnitudes are about half of those predicted by DFT. MEAM potentials predict that the octahedral site will be more stable than the tetrahedral site, while the DFT calculations indicate that both sites will have nearly the same formation energies.

6.3.3 Thermal Properties

To validate the new potential for molecular dynamics simulations, we calculated the melting temperatures of pure Mg crystals. We followed a single-phase method as described by Kim and Tománek [46], in which the temperature is increased at a constant rate and the internal energy of the system is monitored. Fig. 6.2 shows the internal energies of the Mg crystal in the hcp structure as a function of temperature. The plot was obtained from the ensemble average of five hcp structures containing 448 Mg atoms. The initial velocity vectors were set randomly according to the Maxwell-Boltzmann velocity distribution at $T = 100$ K. The temperature of the system was controlled by using a Nosé-Hoover thermostat [35, 73]. It is clearly seen from Fig. 6.2 that the internal energy curve makes an abrupt transition from one linear region to another, marking the melting point. Using this method, we obtained 920 K as the melting temperature of Mg crystals. This result is in good agreement with the experimental value of 923 K. Our result represents a substantial improvement in accuracy from 745 K obtained from a previously published EAM potential [59] or 780 K from a MEAM potential [42]. This so-called single-phase method for melting temperature calculation has a tendancy to cause superheating and over-

estimation of the melting temperature [60]. Although one can use much more elaborate procedures such as a two-phase method [7, 8, 72] to improve our estimation, obtaining an accurate melting point is not the main focus of this paper. We can still conclude that the present MEAM potential is better than the Jelinek potential [42] since the single-phase method should give an upper limit of the melting point.

6.4 Conclusions

In this section we reviewed semi-empirical potential methods for metals including EAM and MEAM. We also reviewed the procedures to construct these potentials. We developed a multi-objective optimization procedure to construct MEAM potentials with minimal manual fitting. We successfully applied this procedure to develop a set of MEAM parameters for the Mg interatomic potential based on first-principles calculations within DFT. The validity and transferability of the new MEAM potentials were tested rigorously by calculating the physical properties of the Mg systems in many different atomic arrangements such as bulk, surface, point defect structures, and molecular dynamics simulations. The new MEAM potential shows a significant improvement over previously published potentials, especially for the atomic forces and melting temperature calculations.

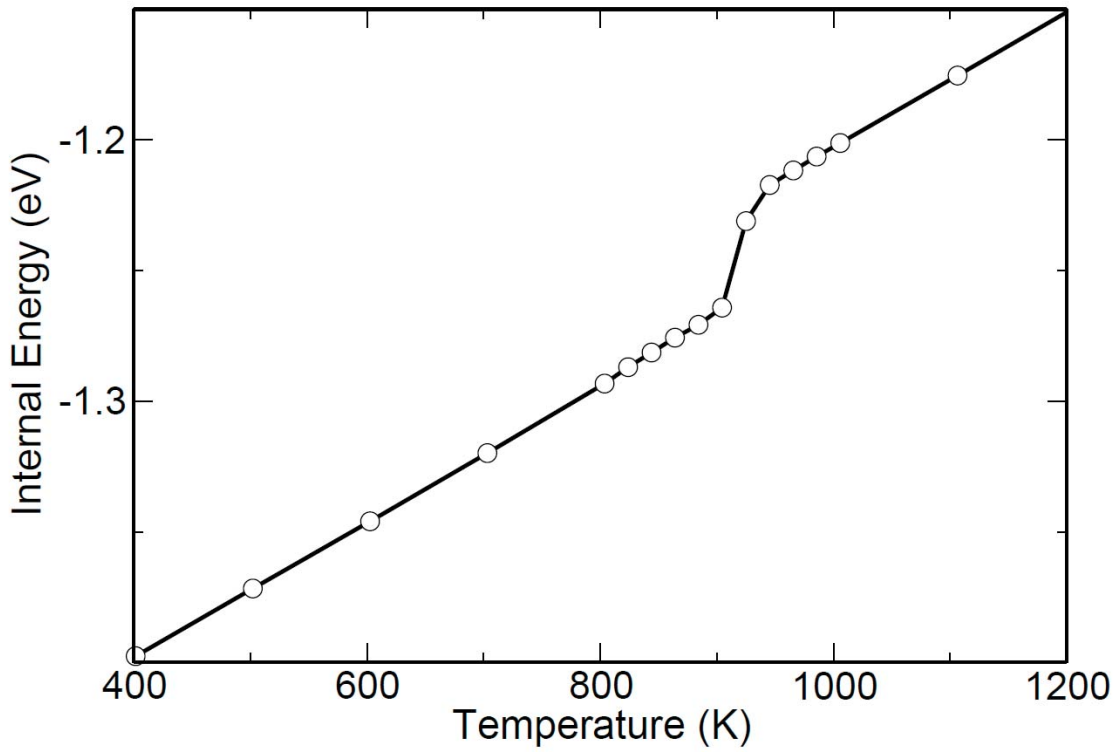

Figure 6.2 Energy vs temperature for the Mg potential.

The internal energies of Mg crystal in hcp structure as a function of temperature. The energies are obtained from the ensemble average of the MD simulations of five structures containing 448 Mg atoms.

CHAPTER 7

CONCLUSION

7.1 Summary

We showed that previously published models for GaSb under extreme Sb-rich growth conditions needed refining due to not being energetically favored compared to the c(4×4) common among other III-V(001) surfaces. We proposed that Ga atoms should be present in the first sublayer of the (001) surface. We supported this based on lower surface energy and in recreating a slight asymmetry present in the experimental STM image with a simulated image from the proposed structural model. The sublayer Ga theory has been supported recently by comparison to experimental reflectance anisotropy spectra. The previously proposed crystal structure of Al-Mg-Zn Φ has been supported by our DFT calculations. The very large and complicated crystal structure makes it nearly impossible to determine exactly which locations should be occupied by Al or Zn even without considering point substitutions. We give the information necessary to reconstruct ten arrangements that were lowest in energy. The many possible vacancy assisted diffusion paths of Fe within Cementite were calculated. A method for optimizing MEAM potentials was developed and applied to improve an existing Mg MEAM potential. It is immediately applicable to other elements with HCP crystal ground states. A moderate amount of recoding would be required to optimize other crystal structures.

7.2 Future Direction

The GaSb surface reconstruction question appears to be solved, but no one has tested the sublayer Ga hypothesis against the double layer (2×10) reconstruction. Our results of Al-Mg-Zn assumed symmetrically equivalent sites were occupied by the same element. This was necessary to make to number of configurations tractable to just brute force calculating them all. Some advanced statistical method could further resolve possible configurations. The results thus far provide a sufficient amount of configurations to be used in developing a ternary Al-Mg-Zn (M)EAM potential. The results from diffusion in Cementite should also be used in development of an Fe-C (M)EAM potential. The method used in optimizing the Mg MEAM potential would benefit from more sophisticated optimizer, especially in limiting the range on MEAM parameters. It also needs to be adapted to other crystal structures.

REFERENCES

[1] J. D. Althoff, P. B. Allen, R. M. Wentzcovitch, and J. A. Moriarty, "Phase diagram and thermodynamic properties of solid magnesium in the quasiharmonic approximation," *Phys. Rev. B*, vol. 48, no. 18, Nov 1993, pp. 13253–13260.

[2] J. Andersson, *Multiobjective Optimization in Engineering Design – Applications to Fluid Power Systems*, doctoral dissertation, Linköping University, Linköping, Sweden, 2001.

[3] M. I. Baskes, "Application of the Embedded-Atom Method to Covalent Materials: A Semiempirical Potential for Silicon," *Phys. Rev. Lett.*, vol. 59, no. 23, Dec 1987, pp. 2666–2669.

[4] M. I. Baskes, "Modified embedded-atom potentials for cubic materials and impurities," *Phys. Rev. B*, vol. 46, no. 5, Aug 1992, pp. 2727–2742.

[5] M. I. Baskes and R. A. Johnson, "Modified embedded atom potentials for HCP metals," *Modell. Simul. Mater. Sci. Eng.*, vol. 2, no. 1, 1994, pp. 147–163.

[6] M. I. Baskes, J. S. Nelson, and A. F. Wright, "Semiempirical modified embedded-atom potentials for silicon and germanium," *Phys. Rev. B*, vol. 40, no. 9, Sep 1989, pp. 6085–6100.

[7] A. B. Belonoshko, "Molecular dynamics of MgSiO3 perovskite at high pressures: Equation of state, structure, and melting transition," *Geochimica et Cosmochimica Acta*, vol. 58, no. 19, 1994, pp. 4039–4047.

[8] A. B. Belonoshko, "Triple fcc-bcc-liquid point on the Xe phase diagram determined by the N-phase method," *Physical Review B (Condensed Matter and Materials Physics)*, vol. 78, no. 17, 2008, p. 174109.

[9] P. E. Blöchl, "Projector augmented-wave method," *Phys. Rev. B*, vol. 50, no. 24, Dec 1994, pp. 17953–17979.

[10] L. Bourgeois, B. C. Muddle, and J. F. Nie, "The crystal structure of the equilibrium [Phi] phase in Mg-Zn-Al casting alloys," *Acta Materialia*, vol. 49, no. 14, 2001, pp. 2701 – 2711.

[11] C. D. MacPherson, R. A. Wolkow, C. E. J. Mitchell, and A. B. McLean, "Scanning Tunneling Microscopy Study of InP(100)-(2×4): An Exception to the Dimer Model," *Phys. Rev. Lett.*, vol. 77, 1996, pp. 691–694.

[12] N. Chetty and M. Weinert, "Stacking faults in magnesium," *Phys. Rev. B*, vol. 56, no. 17, 1997, pp. 10844–10851.

[13] J. B. Clark, "Phase Relations in the Magnesium-Rich Region of the Mg-Al-Zn Phase Diagram," *Trans. Am. Soc. Met.*, vol. 53, 1961, pp. 295–306.

[14] D. J. Chadi, "Atomic structure of GaAs(100)-(2×1) and (2×4) reconstructed surfaces," *J. Vac. Sci. Technol. A*, vol. 5, 1987, pp. 834–837.

[15] D. M. Ceperley and B. J. Alder, "Ground State of the Electron Gas by a Stochastic Method," *Phys. Rev. Lett.*, vol. 45, 1980, pp. 566–569.

[16] D. Z.-Y. Ting and T. C. McGill, "Interface roughness effects on transport in tunnel structures," *J. Vac. Sci. Technol. B*, vol. 14, 1996, pp. 2790–2793.

[17] M. S. Daw and M. I. Baskes, "Semiempirical, Quantum Mechanical Calculation of Hydrogen Embrittlement in Metals," *Phys. Rev. Lett.*, vol. 50, no. 17, Apr 1983, pp. 1285–1288.

[18] M. S. Daw and M. I. Baskes, "Embedded-atom method: Derivation and application to impurities, surfaces, and other defects in metals," *Phys. Rev. B*, vol. 29, no. 12, Jun 1984, pp. 6443–6453.

[19] M. S. Daw, S. M. Foiles, and M. I. Baskes, "The embedded-atom method: a review of theory and applications," *Materials Science Reports*, vol. 9, no. 7-8, 1993, pp. 251 – 310.

[20] P. Donnadieu, A. Quivy, T. Tarfa, P. Ochin, A. Dezellus, M. G. Harmelin, P. Liang, H. L. Lukas, H. J. Seifert, F. Aldinger, and G. Effenberg, "On the Crystal Structure and Solubility Range of the Ternary Φ Phase in the Mg-Al-Zn System," *Z. Metallkd*, vol. 88, no. 12, 1997, pp. 911–916.

[21] J. Emsley, *The Elements*, 3rd. edition, Oxford University Press, Oxford, UK, 1998.

[22] F. Ercolessi and J. Adams, "Interatomic potentials from first-principles calculations: the force-matching method," *Europhys. Lett.*, vol. 26, no. 8, Jun 1994, pp. 583–588.

[23] F. Fuchs, U. Weimer, W. Pletschen, J. Schmitz, E. Ahlswede, M. Walther, J. Wagner, and P. Koidl, "High performance InAs/$Ga_{1-x}In_xSb$ superlattice infrared photodiodes," *Appl. Phys. Lett.*, vol. 71, 1997, pp. 3251–3253.

[24] R. M. Feenstra, D. A. Collins, D. Z.-Y. Ting, M. W. Wang, and T. C. McGill, "Interface roughness and asymmetry in InAs/GaSb superlattices studied by scanning tunneling microscopy," *Phys. Rev. Lett.*, vol. 72, no. 17, Apr 1994, pp. 2749–2752.

[25] R. P. Feynman, "Forces in Molecules," *Phys. Rev.*, vol. 56, no. 4, Aug 1939, pp. 340–343.

[26] M. Finnis and J. Sinclair, "A simple empirical N-body potential for transition metals," *Philos. Mag. A*, vol. 50, no. 1, Jul 1984, pp. 45–55.

[27] G. E. Franklin, D. H. Rich, A. Samsavar, E. S. Hirschorn, F. M. Leibsle, T. Miller, and T.-C. Chiang, "Photoemission and scanning-tunneling-microscopy study of GaSb(100)," *Phys. Rev. B*, vol. 41, no. 18, Jun 1990, pp. 12619–12627.

[28] Gerhard Klimeck, Roger Lake, and Daniel K. Blanks, "Role of interface roughness scattering in self-consistent resonant-tunneling-diode simulations," *Phys. Rev. B*, vol. 58, 1998, pp. 7279–7285.

[29] Guo-Xin Qian, Richard M. Martin, and D. J. Chadi, "First-principles study of the atomic reconstructions and energies of Ga- and As-stabilized GaAs(100) surfaces," *Phys. Rev. B*, vol. 38, 1988, pp. 7649–7663.

[30] Q. Han, K. B. K., and V. Srinath, "Design perspectives for creep-resistant magnesium die-casting alloys," *Philos. Mag.*, vol. 84, no. 36, 2005, pp. 3843–3860.

[31] G. Henkelman, B. P. Uberuaga, and H. Jónsson, "A climbing image nudged elastic band method for finding saddle points and minimum energy paths," *The Journal of Chemical Physics*, vol. 113, no. 22, 2000, pp. 9901–9904.

[32] P. Hofmann, K. Pohl, R. Stumpf, and E. W. Plummer, "Geometric structure of Be(10$\bar{1}$0)," *Phys. Rev. B*, vol. 53, no. 20, May 1996, pp. 13715–13719.

[33] C. Hogan, R. Magri, and R. Del Sole, "Spontaneous Formation of Surface Antisite Defects in the Stabilization of the Sb-Rich GaSb(001) Surface," *Phys. Rev. Lett.*, vol. 104, no. 15, Apr 2010, p. 157402.

[34] P. Hohenberg and W. Kohn, "Inhomogeneous Electron Gas," *Phys. Rev.*, vol. 136, no. 3B, Nov 1964, pp. B864–B871.

[35] W. G. Hoover, "Canonical dynamics: Equilibrium phase-space distributions," *Phys. Rev. A*, vol. 31, no. 3, Mar 1985, pp. 1695–1697.

[36] W. Hu, H. Deng, X. Yuan, and M. Fukumoto, "Point–defect properties in HCP rare earth metals with analytic modified embedded atom potentials," *Eur. Phys. J. B*, vol. 34, no. 4, 2003, pp. 429–440.

[37] W. Hu, B. Zhang, B. Huang, F. Gao, and D. J. Bacon, "Analytic modified embedded atom potentials for HCP metals," *J. Phys.: Condens. Matter*, vol. 13, no. 6, 2001, pp. 1193–1213.

[38] M. Igarashi, M. Khantha, and V. Vitek, "N-body interatomic potentials for hexagonal close-packed metals," *Philos. Mag. B*, vol. 63, no. 3, Mar 1991, pp. 603–627.

[39] J. P. Perdew and A. Zunger, "Self-interaction correction to density-functional approximations for many-electron systems," *Phys. Rev. B*, vol. 23, 1981, pp. 5048–5079.

[40] J. Piao, R. Beresford, and W. I. Wang, "Surface structures of the (Al,Ga)Sb system," *J. Vac. Sci. Technol. B*, vol. 8, 1990, pp. 276–278.

[41] J.B. Boos, W. Kruppa, B.R. Bennett, D. Park, S.W. Kirchoefer, R. Bass, and H.B. Dietrich, "AlSb/InAs HEMT's for low-voltage, high-speed applications," *IEEE Trans. Electron Devices*, vol. 45, 1998, pp. 1869–1875.

[42] B. Jelinek, J. Houze, S. Kim, M. F. Horstemeyer, M. I. Baskes, and S.-G. Kim, "Modified embedded-atom method interatomic potentials for the Mg-Al alloy system," *Phys. Rev. B*, vol. 75, no. 5, 2007, p. 054106.

[43] John E. Northrup and Sverre Froyen, "Structure of GaAs(001) surfaces: The role of electrostatic interactions," *Phys. Rev. B*, vol. 50, 1994, pp. 2015–2018.

[44] J.S. Scott, J.P. Kaminski, S.J. Allen, D.H. Chow, M. Lui, and T.Y. Liu, "Terahertz Response of Resonant-Tunneling Diodes," *Surf. Sci.*, vol. 305, 1994, pp. 389–392.

[45] I. Y. Kim and O. L. de Weck, "Adaptive weighted sum method for multiobjective optimization: a new method for Pareto front generation," *Structural and Multidisciplinary Optimization*, vol. 31, no. 2, Feb 2005, pp. 105–116.

[46] S. G. Kim and D. Tománek, "Melting the fullerenes: A molecular dynamics study," *Phys. Rev. Lett.*, vol. 72, 1994, pp. 2418–2421.

[47] C. Kittel, *Introduction to Solid State Physics*, 7th edition, John Wiley & Sons, Inc., Hoboken, NJ, 1996.

[48] W. Kohn and L. J. Sham, "Self-Consistent Equations Including Exchange and Correlation Effects," *Phys. Rev.*, vol. 140, no. 4A, Nov 1965, pp. A1133–A1138.

[49] G. Kresse and J. Furthmüller, "Efficient iterative schemes for ab initio total-energy calculations using a plane-wave basis set," *Phys. Rev. B*, vol. 54, no. 16, Oct 1996, pp. 11169–11186.

[50] G. Kresse and J. Furthmüller, "Efficient iterative schemes for ab initio total-energy calculations using a plane-wave basis set," *Phys. Rev. B*, vol. 54, no. 16, Oct 1996, pp. 11169–11186.

[51] G. Kresse and J. Hafner, "Ab initio molecular dynamics for liquid metals," *Phys. Rev. B*, vol. 47, no. 1, Jan 1993, pp. 558–561.

[52] G. Kresse and J. Hafner, "Norm-conserving and ultrasoft pseudopotentials for first-row and transition elements," *Journal of Physics: Condensed Matter*, vol. 6, no. 40, 1994, pp. 8245–8257.

[53] G. Kresse and J. Hafner, "Norm-conserving and ultrasoft pseudopotentials for first-row and transition elements," *J. Phys.: Cond. Matt.*, vol. 6, no. 40, 1994, pp. 8245–8257.

[54] G. Kresse and D. Joubert, "From ultrasoft pseudopotentials to the projector augmented-wave method," *Phys. Rev. B*, vol. 59, no. 3, Jan 1999, pp. 1758–1775.

[55] L. J. Whitman, P. M. Thibado, S. C. Erwin, B. R. Bennett, and B. V. Shanabrook, "Metallic III-V (001) Surfaces: Violations of the Electron Counting Model," *Phys. Rev. Lett.*, vol. 79, 1997, pp. 693–696.

[56] H. M. Ledbetter, "Elastic properties of zinc: A compilation and a review," *Journal of Physical and Chemical Reference Data*, vol. 6, no. 4, 1977, pp. 1181–1203.

[57] Y. Li, D. J. Siegel, J. B. Adams, and X.-Y. Liu, "Embedded-atom-method tantalum potential developed by the force-matching method," *Phys. Rev. B*, vol. 67, no. 12, Mar 2003, p. 125101.

[58] P. Liang, T. Tarfa, J. A. Robinson, S. Wagner, P. Ochin, M. G. Harmelin, H. J. Seifert, H. L. Lukas, and F. Aldinger, "Experimental investigation and thermodynamic calculation of the Al-Mg-Zn system," *Thermochimica Acta*, vol. 314, no. 1-2, 1998, pp. 87 – 110.

[59] X.-Y. Liu, J. B. Adams, F. Ercolessi, and J. A. Moriarty, "EAM potential for magnesium from quantum mechanical forces," *Modell. Simul. Mater. Sci. Eng.*, vol. 4, no. 3, 1996, pp. 293–303.

[60] S.-N. Luo, T. J. Ahrens, T. Çağ ın, A. Strachan, W. A. Goddard, and D. C. Swift, "Maximum superheating and undercooling: Systematics, molecular dynamics simulations, and dynamic experiments," *Phys. Rev. B*, vol. 68, no. 13, Oct 2003, p. 134206.

[61] M. C. Righi, Rita Magri, and C. M. Bertoni, "First-principles study of Sb-stabilized GaSb(001) surface reconstructions," *Phys. Rev. B*, vol. 71, 2005, p. 75323.

[62] M. D. Pashley, "Electron counting model and its application to island structures on molecular-beam epitaxy grown GaAs(001) and ZnSe(001)," *Phys. Rev. B*, vol. 40, 1989, pp. 10481–10487.

[63] M. J. Yang, W. J. Moore, B. R. Bennett, and B. V. Shanabrook, "Growth and characterisation of InAs/InGaSb/InAs/AlSb infrared laser structures," *Electron. Lett.*, vol. 34, 1998, pp. 270–272.

[64] M. T. Sieger, T. Miller, and T.-C. Chiang, "Reflection high-energy electron diffraction and photoemission study of GaSb(100) reconstructions," *Phys. Rev. B*, vol. 52, 1995, pp. 8256–8265.

[65] M. J. Mehl, B. M. Klein, and D. A. Papaconstantopoulos, "First-Principles Calculation of Elastic Properties of Metals," *Intermetallic Compounds: Principles and Applications*, J. H. Westbrook and R. L. Fleischer, eds., vol. I, John Wiley & Sons Ltd., London, 1994, pp. 195–210.

[66] M. I. Mendelev, S. Han, W. joon Son, G. J. Ackland, and D. J. Srolovitz, "Simulation of the interaction between Fe impurities and point defects in V," *Phys. Rev. B*, vol. 76, no. 21, 2007, p. 214105.

[67] M. Methfessel and A. T. Paxton, "High-precision sampling for Brillouin-zone integration in metals," *Phys. Rev. B*, vol. 40, no. 6, Aug 1989, pp. 3616–3621.

[68] Y. Mishin, D. Farkas, M. J. Mehl, and D. A. Papaconstantopoulos, "Interatomic potentials for monoatomic metals from experimental data and ab initio calculations," *Phys. Rev. B*, vol. 59, no. 5, Feb 1999, pp. 3393–3407.

[69] Mitsuaki Yano, Hisakazu Yokose, Yoshio Iwai, and Masataka Inoue, "Surface reaction of III-V compound semiconductors irradiated by As and Sb molecular beams," *J. Vac. Sci. Technol. B*, vol. 111, 1991, pp. 609–613.

[70] H. J. Monkhorst and J. D. Pack, "Special points for Brillouin-zone integrations," *Phys. Rev. B*, vol. 13, no. 12, Jun 1976, pp. 5188–5192.

[71] H. J. Monkhorst and J. D. Pack, "Special points for Brillouin-zone integrations," *Phys. Rev. B*, vol. 13, no. 12, Jun 1976, pp. 5188–5192.

[72] J. R. Morris, C. Z. Wang, K. M. Ho, and C. T. Chan, "Melting line of aluminum from simulations of coexisting phases," *Phys. Rev. B*, vol. 49, no. 5, Feb 1994, pp. 3109–3115.

[73] S. Nosé, "A unified formulation of the constant temperature molecular dynamics methods," *J. Chem. Phys.*, vol. 81, no. 1, 1984, pp. 511–519.

[74] D. J. Oh and R. A. Johnson, "Simple embedded atom method model for fec and hcp metals," *J. Mater. Res.*, vol. 3, no. 3, 1988, pp. 471–478.

[75] V. Pareto, *Manuale di Economia Politica*, Societa Editrice Libraria, 1909, Translated into English by A.S. Schwier as *Manual of Political Economy*, Macmillan, New York, 1971.

[76] R. Pasianot and E. J. Savino, "Embedded-atom-method interatomic potentials for hcp metals," *Phys. Rev. B*, vol. 45, no. 22, Jun 1992, pp. 12704–12710.

[77] G. Pettersen, H. Westergen, R. Hoier, and L. O., "Microstructure of a pressure die cast magnesium—4wt.% aluminium alloy modified with rare earth additions," *Mater. Sci. Eng. A*, vol. 207, 1996, pp. 115–120.

[78] W. H. Press, B. P. Flannery, S. A. Teukolsky, and W. T. Vetterling, *Numerical Recipes in C: The Art of Scientific Computing*, second edition, Cambridge University Press, Cambridge, 1992.

[79] V. Raghavan, "Al-Mg-Zn (Aluminum-Magnesium-Zinc)," *Journal of Phase Equilibria and Diffusion*, vol. 28, 2007, pp. 203 – 208.

[80] J. H. Rose, J. R. Smith, F. Guinea, and J. Ferrante, "Universal features of the equation of state of metals," *Phys. Rev. B*, vol. 29, no. 6, Mar 1984, pp. 2963–2969.

[81] S. B. Zhang and Alex Zunger, "Method of linear combination of structural motifs for surface and step energy calculations: Application to GaAs(001)," *Phys. Rev. B*, vol. 53, 1996, pp. 1343–1356.

[82] J.-H. Shim, B.-J. Lee, and Y. Cho, "Thermal stability of unsupported gold nanoparticle: a molecular dynamics study," *Surface Science*, vol. 512, 2002, pp. 262–268.

[83] C. J. Smith, ed., *Metal Reference Book*, 5th edition, Butterworth, Lodon, UK, 1976.

[84] P. Staikov and T. S. Rahman, "Multilayer relaxations and stresses on Mg surfaces," *Phys. Rev. B*, vol. 60, no. 23, Dec 1999, pp. 15613–15616.

[85] The Third China-Japan-Korea Joint Symposium on Optimization of Structural and Mechanical Systems, *Multiobjective Optimization: History and Promise*, Kanazawa, Japan, October 2004.

[86] W. R. Tyson and W. A. Miller, "Surface free energies of solid metals: estimation from liquid surface tension measurements," *Surf. Sci.*, vol. 62, 1977, pp. 267–276.

[87] D. Vanderbilt, "Soft self-consistent pseudopotentials in a generalized engenvalue formalism," *Phys. Rev. B*, vol. 41, 1990, pp. 7892–7895.

[88] S. W., "A survey of multicriteria optimization, or the vector maximum problem," *J. of Optimization Theory and Applications*, vol. 29, 1979, pp. 1–52.

[89] W. Barvosa-Carter, A.S. Bracker, J.C. Culbertson, B.Z. Nosho, B.V. Shanabrook, L.J. Whitman, Hanchul Kim, N.A. Modine, and E. Kaxiras, "Structure of III-Sb(001) Growth Surfaces: The Role of Heterodimers," *Phys. Rev. Lett.*, vol. 84, 2000, pp. 4649–4652.